4

Quarterly Technical Report

Growth, Characterization and Device Development in Monocrystalline Diamond Films

Supported under Grant #N00014-93-I-0437
Office of the Chief of Naval Research
Report for the period 10/1/93–12/31/93

R. F. Davis, J. T. Glass, and R. J. Nemanich*
K. S. Ailey, P. K. Baumann*, L. Bergman*, D. J. Kester,
D. J. Lichtenwalner, M. T. McClure, F. R. Sivazlian, B. R. Stoner,
J. van der Weide*, M. G. Wensell*, S. D. Wolter, and Z. Zhang*
North Carolina State University
c/o Materials Science and Engineering Department
*Department of Physics
Raleigh, NC 27695

December, 1993

REPORT DOCUMENTATION PAGE

Form Approved
OMB No. 0704-0188

1. AGENCY USE ONLY (Leave blank)	2. REPORT DATE	3. REPORT TYPE AND DATES COVERED
	December, 1993	Quarterly Technical 10/1/93–12/31/93

4. TITLE AND SUBTITLE

Growth, Characterization and Device Development in Monocrystalline Diamond Films

5. FUNDING NUMBERS

s400003srr14
1114SS
N00179
N66005
4B855

6. AUTHOR(S)

Robert F. Davis, J. T. Glass and R. J. Nemanich

7. PERFORMING ORGANIZATION NAME(S) AND ADDRESS(ES)

North Carolina State University
Hillsborough Street
Raleigh, NC 27695

8. PERFORMING ORGANIZATION REPORT NUMBER

N00014-93-I-0437

9. SPONSORING/MONITORING AGENCY NAMES(S) AND ADDRESS(ES)

Sponsoring: ONR, Code 314, 800 N. Quincy, Arlington, VA 22217-5660
Monitoring: Office of Naval Research Resider
The Ohio State University Research Center
1960 Kenny Road
Columbus, OH 43210-1063

10. SPONSORING/MONITORING AGENCY REPORT NUMBER

11. SUPPLEMENTARY NOTES

12a. DISTRIBUTION/AVAILABILITY STATEMENT

Approved for Public Release; Distribution Unlimited

12b. DISTRIBUTION CODE

13. ABSTRACT *(Maximum 200 words)*

Biased enhanced nucleation of diamond on β-SiC(100) and Si(100) has been achieved but not on Cu(100). Carbide formation is an apparent attribute to the nucleation. The refractory metals of Hf, Ti, Ta, Ni and W were thus explored as substrates. Diamond nucleation density was found to be directly related to the carbide heat of formation without scratching these substrates. TEM of highly oriented diamond films on Si(100) showed dislocations at low angle boundaries formed from coalesced grains. The azimuthal rotation between grains was between 0–6°. Negative electron affinity (NEA) has been found experimentally and theoretically for the 2×1 reconstructed diamond surface. Theoretical results indicate that the observed NEA is associated with a monohydride terminated surface, while the hydrogen-free surface exhibits a positive electron affinity. Raman and various photoluminescence (PL) techniques were used to investigate the role of N doping on the optical centers in CVD diamond films. The PL transitions attributed to the zero-phonon lines of N centers are observed at 1.945 eV and 2.154 eV. A new N center at 1.967 eV and the band A luminescence were also observed. The presence of an in-gap state distribution resulting from the sp^2 disordered phase has been established. BN films have been grown on [100] oriented Si, diamond, Cu and Ni substrates via IBAD and characterized via FTIR and HRTEM. The film consisted of the growth sequence of a-, h-, and c-BN and is attributed primarily to increasing compressive intrinsic stress and increased film thickness.

14. SUBJECT TERMS

diamond, bias-enhanced nucleation, heteroepitaxial growth, refractory metals, β-SiC(100), Si(100), TEM, grain boundaries, negative electron affinity, Raman, photoluminescence, N centers, BN films, cubic BN, intrinsic stress

15. NUMBER OF PAGES

63

16. PRICE CODE

17. SECURITY CLASSIFICATION OF REPORT	18. SECURITY CLASSIFICATION OF THIS PAGE	19. SECURITY CLASSIFICATION OF ABSTRACT	20. LIMITATION OF ABSTRACT
UNCLAS	UNCLAS	UNCLAS	SAR

Table of Contents

I. Introduction

Diamond as a semiconductor in high-frequency, high-power transistors has unique advantages and disadvantages. Two advantages of diamond over other semiconductors used for these devices are its high thermal conductivity and high electric-field breakdown. The high thermal conductivity allows for higher power dissipation over similar devices made in Si or GaAs, and the higher electric field breakdown makes possible the production of substantially higher power, higher frequency devices than can be made with other commonly used semiconductors.

In general, the use of bulk crystals severely limits the potential semiconductor applications of diamond. Among several problems typical for this approach are the difficulty of doping the bulk crystals, device integration problems, high cost and low area of such substrates. In principal, these problems can be alleviated via the availability of chemically vapor deposited (CVD) diamond films. Recent studies have shown that CVD diamond films have thermally activated conductivity with activation energies similar to crystalline diamonds with comparable doping levels. Acceptor doping via the gas phase is also possible during activated CVD growth by the addition of diborane to the primary gas stream.

The recently developed activated CVD methods have made feasible the growth of polycrystalline diamond thin films on many non-diamond substrates and the growth of single crystal thin films on diamond substrates. More specifically, single crystal epitaxial films have been grown on the {100} faces of natural and high pressure/high temperature synthetic crystals. Crystallographic perfection of these homoepitaxial films is comparable to that of natural diamond crystals. However, routes to the achievement of rapid nucleation on foreign substrates and heteroepitaxy on one or more of these substrates has proven more difficult to achieve. This area of study has been a principal focus of the research of this contract.

At present, the feasibility of diamond electronics has been demonstrated with several simple experimental devices, while the development of a true diamond-based semiconductor materials technology has several barriers which a host of investigators are struggling to surmount. It is in this latter regime of investigation that the research described in this report has and continues to address.

In this reporting period, biased enhanced nucleation of diamond on the substrates of β-SiC(100), Si(100), Cu(100) and the refractory metals of Hf, Ti, Ta, Ni and W has been investigated. Transmission electron microscopy has been used to study the defects at the low angle boundaries between coalesced grains of highly oriented grains. Both experimental and theoretical studies have been conducted regarding the negative electron affinity effect on monohydride terminated diamond surfaces. Raman and various photoluminescence (PL) techniques have been used to investigate the role of N doping on the optical centers in CVD diamond films. Finally, boron-nitride films have been grown on [100] oriented Si, diamond,

Cu and Ni substrates via ion beam assisted deposition and characterized via FTIR and HRTEM.

The following subsections detail the experimental procedures for each of the aforementioned studies, discuss the results and provide conclusions and references for these studies. Note that each major section is self-contained with its own figures, tables and references.

II. Bias-enhanced Nucleation on Refractory Metal Substrates

A. Introduction

The first attempts to produce synthetic diamond relied upon the fact that diamond is composed entirely of carbon. Therefore, to form diamond it is essential that for the case of low pressure CVD, for example, a carbon containing gas source is utilized. In this high temperature process environment it is likely that carbide phases will be produced if the substrates are capable of forming them. These carbide phases have been observed via x-ray diffraction (XRD) [1] and surface sensitive techniques [2, 3] such as x-ray photoelectron spectroscopy (XPS) and Auger electron spectroscopy (AES).

The understanding how the formation of a carbide influences the diamond nucleation process is important. Joffreau *et al.* [1] have observed an influence on diamond nucleation pertaining to refractory metal substrates. These substrates are known carbide formers and their formation was confirmed via XRD. Also, surface analytical studies on scratched silicon have indicated the formation of a carbide prior to detecting the presence of diamond [2, 3]. It should be noted though that very early during nucleation the presence of diamond may be difficult to observe since the diamond present is possibly below the sensitivity of the analytical instrumentation. To enhance the nucleation density on these and other non-carbide forming substrates the typical pretreatment involves scratching the substrates with diamond grit. Researchers suggest that diamond residue from this pretreatment routine is important for diamond nucleation [4, 5]. This diamond residue may act as nucleation sites and/or may provide surface carbon that is ideal for diamond nucleation. The form of the surface carbon may be relevant for diamond nucleation; therefore, much work has been directed toward observing the influence of nucleation on the form of the surface carbon [5–7]. It appears that the form of the surface carbon and the formation of a carbide play a role in the diamond nucleation process.

This study was undertaken to investigate the influence of bias-enhanced nucleation (BEN) on the refractory metals. BEN has been observed to enhance the diamond nucleation density on unscratched silicon substrates [8, 9]. This process involves applying a negative bias to the substrate holder in order to promote diamond nucleation. The carbide forming nature of silicon has been speculated to be an important attribute of this material [8, 10]. Thus, the varying degrees of the carbide forming nature of the refractory metals may indicate a correlation with the nucleation phenomena via BEN. This should make it possible to gain further insight into the BEN phenomena as well as investigating potential heteroepitaxial substrates using this pretreatment technique.

B. Experimental

Bias-enhanced nucleation of diamond and diamond deposition was performed in a microwave plasma CVD chamber purchased from Applied Science and Technology, Inc. The growth system and BEN apparatus has been discussed previously [8]. Table I indicates the BEN and growth conditions utilized in this study. The refractory metals used in this study were hafnium, titanium, tantalum, niobium, and tungsten. These substrates were chosen as arbitrary representations of carbide formers with the exception to hafnium in which this substrate was used to confirm possible correlations as explained in the Discussion section. The substrates were highly polished down to 0.05μm alumina grit suspended in deionized water.

Table I. The BEN and growth conditions utilized in this study

Process Parameters	Bias Conditions	Growth Conditions
Microwave Power	900 Watts	900 Watts
CH_4/H_2	5%	1%
Pressure	15 Torr	25 Torr
Substrate Temperature	~725°C	~700°C
Bias Voltage	-250V_{DC}	Floating
Bias Current	~100mA	N/A
Sample Position	Immersed	Immersed

Alumina was used in the final polishing procedure to ensure that very little residual diamond would be present on the substrates which was used in the preceding polishing steps. The substrates were then solvent cleaned using TCE, acetone, methanol, and 2-propanol, consecutively. A deionized water rinse was performed on the substrates just prior to entering into the growth chamber. As discussed briefly, BEN was used as an *in situ* pretreatment technique to promote diamond nucleation. A negative potential was applied to the molybdenum holder containing the substrate. The positive potential was applied to the chamber wall. The refractory metal substrates were subjected to various bias times followed by 30 minutes of growth to obtain a plot of nucleation density versus bias time. The short growth period enabled an accurate account of all the diamond nuclei that was later determined by scanning electron microscopy (SEM). X-ray diffraction (XRD) was used to determine the phases present following BEN and the short growth period. Table II lists the carbide phases observed via XRD in addition to their carbide heat of formation values [11].

Table II. This table indicates the metal-carbides observed in this study using XRD. Along with this data are the carbide heat of formation for each.

Possible Carbides	ΔH_f (kcal/mole-metal)	Observed in this study
β-SiC	-15.6	Not studied
HfC	-60.1	Yes
TiC	-44.1	Yes
TaC	-35.0	Yes
Ta_2C	-24.9	Yes
NbC	-33.2	Yes
Nb_2C	-23.3	Yes
WC	-9.69	Yes
W_2C	-3.2	Yes

C. Results

The plot of nucleation density versus bias time for the refractory metals referenced to silicon and copper is shown in Fig. 1. A study of copper versus silicon revealed that the substrate choice did influence the nucleation density during BEN [10]. This is obvious as indicated in this plot. The individual plots for the refractory metals were fit with correlation coefficients greater than 0.85. The influence that BEN had on these substrates was determined by denoting the nucleation densities at 60 minutes of biasing. At this time the nucleation densities were approximately constant with any further biasing. The nucleation densities at these times are plotted in Fig. 2 according to there position in the refractory metal portion of the periodic table. This plot suggests that there is a correlation established among these materials. The metals in parenthesis are estimated positions as related to the substrates studied in this report.

The materials under investigation as discussed earlier were hafnium, titanium, tantalum, niobium, and tungsten. The hafnium, though, was studied following the work on the other metals to verify the possible correlation existing among these metals as was indicated in Fig. 2. It was determined in research conducted by Joffreau *et al.* [1] that the substrate may influence diamond nucleation. In their study refractory substrates displayed a correlation to the incubation time (i.e. the time prior to the onset of nucleation) and the nucleation rate. Therefore, it is not unlikely that the refractory metals in this study also show a correlation. The correlation to the material properties of these metals referenced to the nucleation density via BEN will be discussed in the next section.

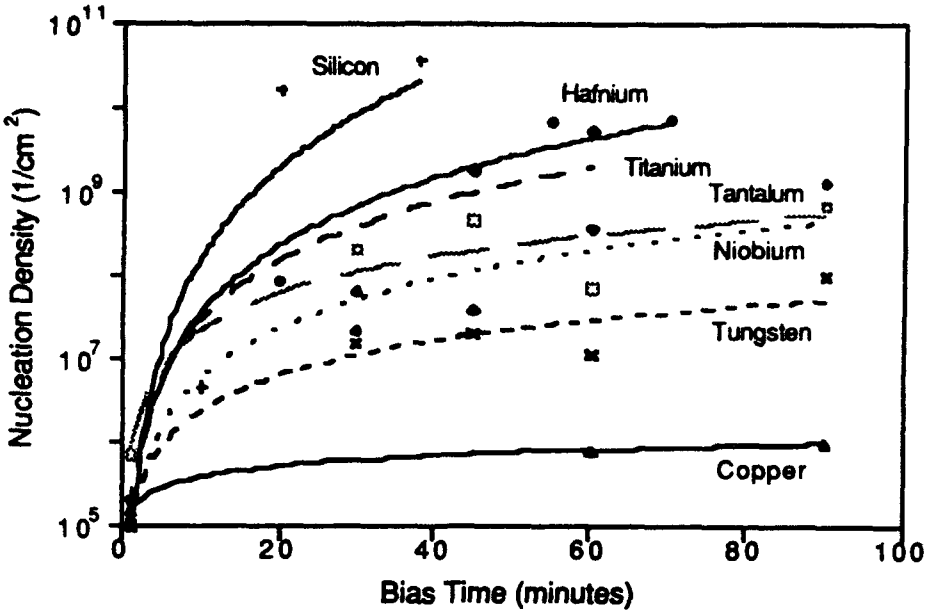

Figure 1. This plot illustrates the relative influence of BEN on the refractory metal substrates referenced to silicon and copper.

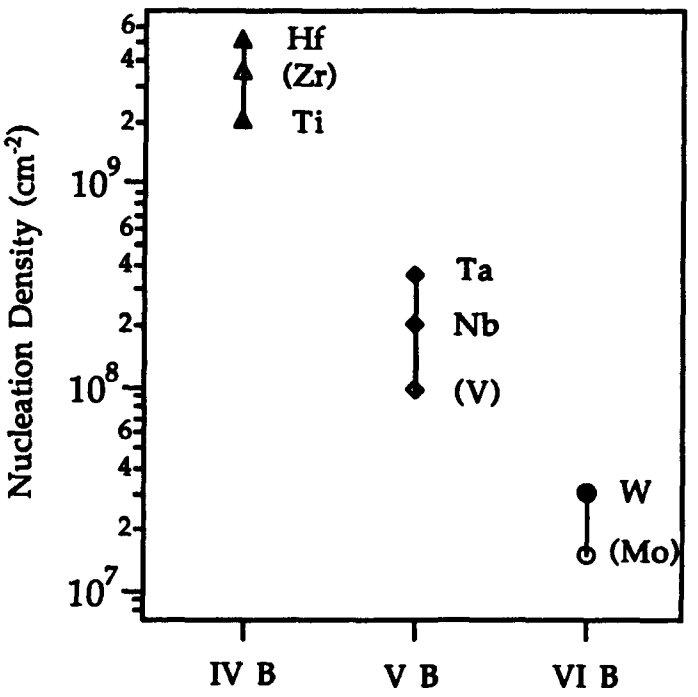

Figure 2. This graphic shows the nucleation density at 60 minutes of biasing according to the relative positions of the refractory metals in the periodic table.

The refractory metals that were targeted are shown in Fig. 3 as they are situated in the periodic table. These materials were chosen because of their carbide forming nature. A previous study of copper versus silicon indicated a substrate effect [10]; the carbide forming nature of silicon was believed to be a key factor. The choice of these metals also allowed a group of materials to be studied with the possibility of observing other properties of these substrates which could enhance the effects of BEN. The study of refractory metals and refractory metal carbides have been undertaken for decades with the intent to investigate their high temperature material characteristics. Figure 4 shows a trend established between the activation energy for carbon diffusion in the refractory metal substrates and the melting points of these refractory metals [11].

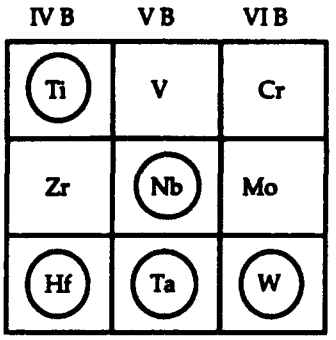

Figure 3. The refractory metals used in this study are indicated in their respective position in the periodic table.

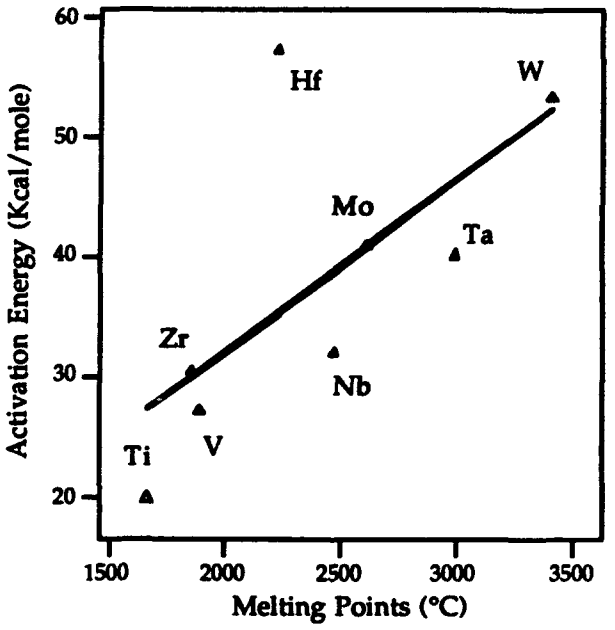

Figure 4. This figure notes the trend between the activation energy for diffusion of carbon in the refractory metal substrates versus their melting points [11].

Also, Fig. 5 shows a correlation between the carbide heat of formation and the ratio of the melting points of the metal to that of the metal carbide [11]. This later figure was based on the work by Worrel *et al.* [12] It can be assumed then that in reference to Fig. 4 the carbon diffusivity in the refractory metals is related to the melting points of these metals. Also, the thermodynamic relationship presented by Worrel gives some indication as to the metal-carbon bonding nature. The carbide heat of formation related to the refractory metals in their respective groups in the periodic table are shown in Fig. 6. This data shows the distinct correlation among the refractory metals for this thermodynamic property. The carbide data obtained from the literature are difficult to determine and the data in some instances are still not well established. Therefore, the overall trends presented in this work are emphasized with little emphasis placed on the specific values. Figure 7 indicates the trend established in the present study between the carbide heat of formation and the nucleation density at 60 minutes of biasing.

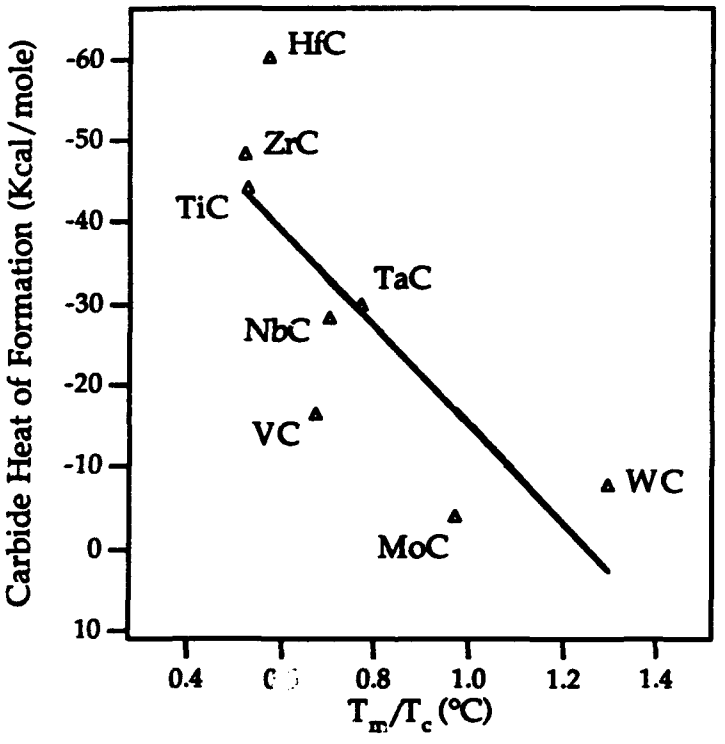

Figure 5. This graphic indicates a correlation between the carbide heat of formation and the ratio of the metal to metal-carbide melting points.

E. Conclusions

BEN has lead to heteroepitaxy on β-SiC [13, 14] and Si(100) [15]. A BEN study conducted on copper showed a slight influence for enhancing the nucleation density [10].

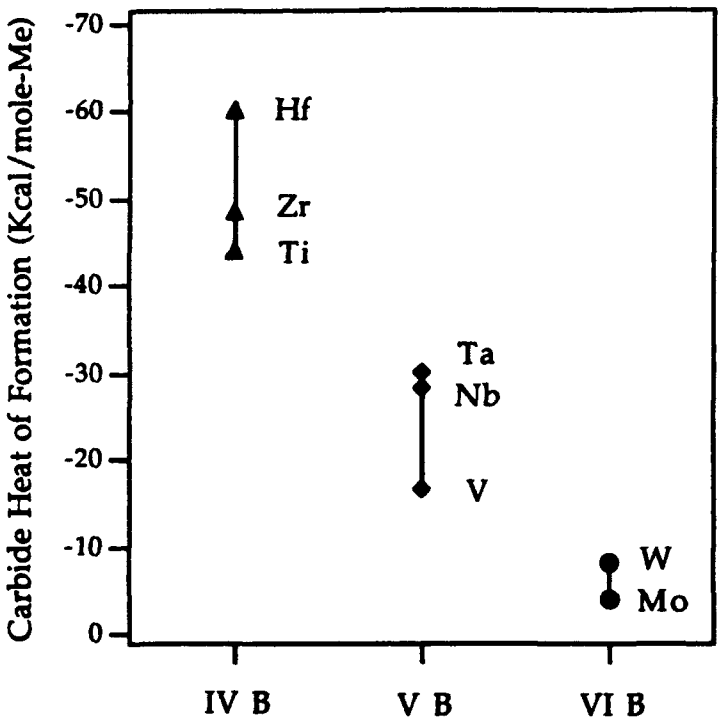

Figure 6. Material properties such as the carbide heat of formation as is shown here illustrates a correlation among the refractory metals.

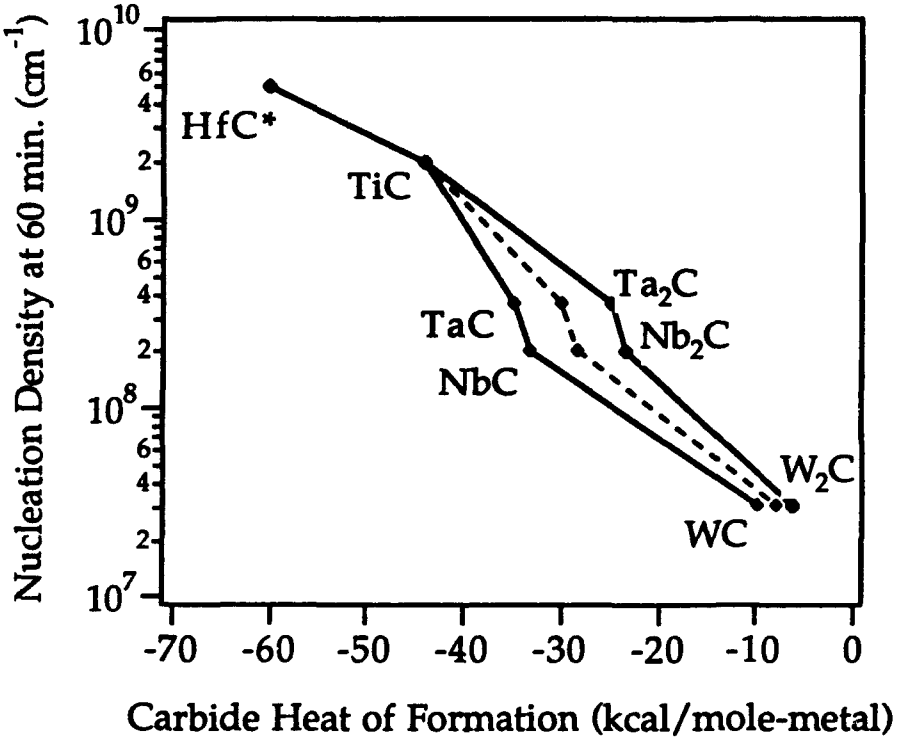

Figure 7. The trend established in the present study between the carbide heat of formation and the nucleation density at 60 minutes of biasing.

Therefore, the carbide forming nature of silicon appears to be an important attribute. Thus, the motivation for studying the refractory metals is linked to their carbide forming traits. These substrates offer a class of potential heteroepitaxial substrates and also provide a group of metals that because they possess different material properties are ideal for gaining an understanding of BEN. The refractory metals did show a correlation to the carbide heat of formation. This property have been discussed to be related to other refractory material properties. The thermodynamic data referenced to the nucleation density at 60 minutes of biasing indicates very strongly that the substrates are influencing the nucleation mechanisms, as was the case in the study of BEN on copper. Also, the relatively high nucleation densities (with no scratching pretreatment) reveals that, provided a high quality carbide may be formed, these substrates are potential candidates for BEN of heteroepitaxial diamond.

F. Acknowledgments

The authors wish to acknowledge the financial support of this research which was provided in part by BMDO/IST through ONR and the Kobe Steel, Ltd. Professorship at NCSU.

G. References

1. P. O. Joffreau, R. Haubner and B. Lux, Int. J. of Ref. Hard Metals, **7** (1988) 186.
2. D. N. Belton, S. J. Harris, S. J. Schmieg, A. M. Wiener and T. A. Perry, Appl. Phys. Lett., **54** (1989) 416.
3. B. E. Williams, B. R. Stoner, D. A. Asbury and J. T. Glass, presented at *NATO Advanced Study Institute on Diamond and Diamond-Like Films and Coatings*, Castelvecchio Pascoli, Italy, 1990.
4. P. K. Bachmann, W. Drawl, D. Knight, R. Weimer and R. F. Messier, presented at *Diamond and Diamond-Like Materials Synthesis , 1988*, Materials Research Society, p. 99.
5. J. C. Angus, Z. Li, M. Sunkara, R. Gat, A. B. Anderson, S. P. Mehandru and M. W. Geis, *Proceedings of the Second International Symposium on Diamond Materials*, Electrochemical Society Meeting, Washington, DC, May 5-10, 1991.
6. J. J. Dubray, C. G. Pantano, M. Meloncelli and E. Bertran, J. Vac. Sci. Technol. A, **9** (1991) 3012.
7. Y. Avigal, Diamond and Related Materials, **1** (1992)
8. B. R. Stoner, G.-H. M. Ma, S. D. Wolter and J. T. Glass, Phys. Rev. B, **45** (1991) 11067.
9. S. Yugo, T. Kanai, T. Kimura and T. Muto, Appl. Phys. Lett., **58** (1991) 1036.
10. S. D. Wolter, B. R. Stoner and J. T. Glass, Diamond and Related Materials, (1994), in press.
11. *CRC Handbook of Chemistry and Physics*, CRC Press, Inc., Boca Raton, 1983-1984.
12. W. L. Worrell, J. Phys. Chem., **68** (1964) 954.
13. B. R. Stoner and J. T. Glass, Appl. Phys. Lett., **60** (1992) 698.
14. B. R. Stoner, G. H. Ma, S. D. Wolter, W. Zhu, Y.-C. Wang, R. F. Davis and J. T. Glass, Diamond and Related Materials, **2** (1993) 142.
15. S. D. Wolter, B. R. Stoner, J. T. Glass, P. J. Ellis, D. S. Buhaenko, C. E. Jenkins and P. Southworth, Appl. Phys. Lett., **62** (11) (1993) 1215.

III. Investigation of the Low Angle Grain Boundaries in Highly Oriented Diamond Films via Transmission Electron Microscopy*

F. R. Sivazlian, J. T. Glass
Dept. of Materials Science, North Carolina State University, Raleigh, NC 27695-7919
and
B. R. Stoner
Kobe Steel USA, Inc., Electronic Materials Center, Research Triangle Park, NC 27209

Highly oriented diamond thin films grown on silicon via microwave plasma chemical vapor deposition were examined by transmission electron microscopy. In the plan view, defects appearing at the grain boundary were easily observed. (100) faceted grains that appeared to have coalesced were connected at their interfaces by dislocations characteristic of a low angle grain boundary. From Burgers vector calculations and electron diffraction patterns, the azimuthal rotation between grains was measured to be between 0 and 6 degrees. The defect densities of these films are compared to reports from (100) textured randomly oriented films and the relative improvement due to the reduction of misorientation and grain boundary angles will be discussed.

*Submitted to Journal of Materials Research

Diamond thin films are attractive for numerous applications involving electronic devices in extreme environments due to several unique properties [1]. At the moment, this goal is limited by the unavailability of low cost single crystal diamond; however, synthetic diamond grown via chemical vapor deposition (CVD) has produced highly oriented polycrystalline diamond [2] which may be sufficient quality to address certain electronic properties. However, a major issue for these oriented polycrystalline films will be the effect of grain boundaries on the resulting electronic properties. Ideally, defects, grain boundaries and roughness will be minimized such that the film properties approach those of single crystal. Structural information regarding the grain boundaries and associated defects could lead to a greater understanding of the basic growth mechanisms and the resulting electronic properties of highly oriented diamond films. Transmission electron microscopy (TEM) is a powerful tool for understanding such defects and grain boundaries. Previous TEM work in diamond has given insight into the diamond/substrate interface [3-9] and defects both within the grains and at the grain boundaries [10-14]. However, no TEM studies to date have been reported on highly oriented diamond films consisting of epitaxially oriented grains.

The (100) oriented diamond films used for these experiments were grown on (100) silicon via bias-enhanced microwave plasma chemical vapor deposition (MPCVD) using a three step growth process, details of which have been previously reported [2]. Plan view TEM was conducted with the transmitted beam parallel to the [001] direction. Sample preparation of these films used a standard technique of polishing and dimpling followed by ion milling until penetration through the film [4].

A TOPCON 002B high resolution microscope operated at 200kV and a Hitachi H-800, also operated at 200kV, were used for these samples. The TOPCON 002B was chosen for its high magnification and microdiffraction capabilities which permitted diffraction pattern imaging from small areas. The grain boundaries were characterized by bright field and dark field images

while the tilt between grains was determined by Burgers vector calculations and selected area electron diffraction (SAD) patterns. Low magnification was used to observe the shape of the diamond particles that had grown together and the defect incorporation over a larger area while high magnification showed details of the defects at the grain boundaries. SAD patterns were taken at the grain boundary and within each individual grain in order to measure the tilt between adjacent grains.

A scanning electron microscope (SEM) image of the diamond film used for this study is shown in figure 1. From this micrograph it is obvious that the grains are highly oriented and many appear to have coalesced, as indicated by the arrows. In previous work on polycrystalline (100) faceted diamond films, various defects including microtwins were observed between the high angle grain boundary regions [9]. A TEM micrograph from the highly oriented film used in this study is shown in figure 2. In this figure, one observes several lines of dislocations, indicative of grain boundaries similar to the ones shown in figure 1. Although most boundaries were parallel to the <110> direction, this micrograph shows boundaries parallel to both the <110> and <100> directions as indicated by the arrows on the micrograph.

Several grain boundaries were observed at high magnification. Figure 3 shows an example of a low angle grain boundary with a series of distinctive dislocations, indicated by the arrows located at every 5th dislocation. The spacing between each of these dislocations is about 20 nm. Although many of the boundaries observed were considered as low angle, a rotation of 2° or less, some boundaries were rotated as much as 6°. In boundaries such as these, the dislocation density increases to accommodate the high misorientation, as a consequence distinct dislocations are not observed.

The rotation between grains was measured via two methods; dislocation spacing and diffraction patterns. In figure 3, the dislocations are widely spaced, indicative of a small degree of rotation. From g•b [15] criteria, the Burgers vector was determined to be a $\frac{1}{2}$<110> type dislocation. The rotation between grains was determined using the expression, $\Theta = \frac{b}{d}$ where Θ is the degree of rotation, b is the Burgers vector and d is the dislocation spacing. The rotation was

calculated to be ≈ 1°, which is consistent with the angle measured from the electron diffraction pattern and verifies the direction of the Burgers vector. Similar results have been reported in GaAs, also with a diamond cubic type structure 16.

Additionally, close examination of the electron diffraction pattern permitted observation of the tilt between the two grains (see inset in figure 3). By moving from one grain to another the {220} diffraction spot was observed to shift slightly, indicative of a misorientation between the two grains. Using the diffraction pattern at the grain boundary, the angle between the two {220} spots indicated by the arrows was measured to give the tilt between the two grains. This result corresponds to the tilt measured by Burgers vector calculations. Several grains were measured and the angle was consistently between 0 and 6 degrees. These measurements corroborate with previous measurements of the misorientation of diamond films on silicon via x-ray pole figure analysis 17 and previous results using cross-sectional TEM of epitaxial diamond on single crystal ß-SiC [9].

For diamond to be a viable material for active electronic devices, relatively defect free single crystal films need to be deposited over reasonably large areas. Clausing and coworkers [11] demonstrated that the density of intragranular planar defects such as twins and stacking faults are much lower for growth on (100) as compared to the {111} planes. Therefore, by growing under conditions which promote (100) texture, these defects will reside primarily at the grain boundaries. With the density of twins and stacking faults reduced, point defects and dislocations become the primary defects affecting the electronic transport properties. In the present work, the defect densities are further reduced by depositing a film that is both (100) textured and highly oriented. This decreases the defect density at the low angle grain boundaries to a series of parallel dislocations. A more coherent boundary occurs which causes less thermal and electronic scattering. This was verified by selectively depositing on the surface of these highly oriented, (100) textured films 17. The resulting mobility represented a factor of 5 improvement over the highest reported values for polycrystalline films but was still approximately 1/3 that of films grown under similar conditions on single crystal substrates. These results suggests that the low

angle grain boundaries and associated defects continue to limit the transport properties of the highly oriented films. For highly oriented films to become viable alternatives to single crystals for active electronic devices, misorientation and the corresponding defects need to be further reduced.

In summary (100) oriented diamond films grown on Si (100) via bias-enhanced MPCVD were examined by transmission electron microscopy in the plan view. Grains examined at low magnification were seen to have grown together to form irregular grain boundaries. At higher magnifications dislocations were observed at grain boundaries, indicative of a low angle grain boundary. To confirm the misorientation, calculations utilizing both the Burgers vector and electron diffraction patterns determined a tilt of $\approx 1^{\circ}$. Several different low angle grain boundaries were observed, the tilt measured between 0 and 6 degrees, varying slightly from grain to grain. These results are consistent with previous measurements by x-ray pole figure analysis and with samples grown on single crystal ß-SiC and suggest that further improvements in heteroepitaxial growth of diamond are warranted before CVD films can realize their full potential as an electronic material.

ACKNOWLEDGMENTS

The authors would like to thank B. Fox from Kobe Steel Ltd., J. Posthill from RTI and W. Zhu from N. C. State for their helpful discussions. Additionally the authors would like to thank Kobe Steel USA Inc. for use of their scanning electron microscope. This research was partially funded by SMDO / IST through ONR.

REFERENCES

1. M. W. Geis, Carbon, **28**, 806 (1990).

2. B. R. Stoner, S. Sahaida, J. P. Bade, P. Southworth and P. J. Ellis, J. Mater. Res., **8**, (1993).

3. A. Argoitia, J. C. Angus, L. Wang, X. I. Ning and P. Pirouz, J. of Appl. Phys., **73**, 4305-4312 (1993).

4. G.-H. M. Ma, Y. H. Lee and J. T. Glass, J. Mater. Res., **5**, 2367-77 (1990).

5. B. E. Williams, D. A. Asbury and J. T. Glass, in *The Physics and Chemistry of Carbides; Nitrides and Borides*, edited by R. Freer, (Kluwer Academic Publishers, Published in the Netherlands, 1990), 169-181.

6. W. Zhu, X. H. Wang, B. R. Stoner, G. H. M. Ma, H. S. Kong, M. W. H. Braun and J. T. Glass, Phys. Rev. B, **47**, 6529-6542 (1993).

7. J. S. Ma, H. Kawarada, T. Yonehara, J. I. Suzuki, J. Wei, Y. Yokota, H. Mori, H. Fujita and A. Hiraki, Appl. Surf. Sci., **41**, 572-579 (1989).

8. B. E. Williams, J. T. Glass, R. F. Davis and K. Kobashi, J. Crys. Growth, **99**, 1168-76 (1990).

9. B. R. Stoner, G. H. Ma, S. D. Wolter, W. Zhu, Y.-C. Wang, R. F. Davis and J. T. Glass, Diamond and Related Materials, **2**, 142-146 (1993).

10. B. E. Williams, J. T. Glass, R. F. Davis, K. Kobashi and Y. Kawate, Extended Abstracts Diamond and Diamond-Like Materials Synthesis, edited by G. H. Johnson, A. R. Badzian and M. W. Geis, (1988), 59-62.

11. R. E. Clausing, L. Heatherly, K. L. More and G. M. Begun, Surf. Coat. Techno., **39/40**, 199 (1989).

12. Z. L. Wang, J. Bentley, R. E. Clausing, L. Heatherly and L. L. Horton, Applications of Diamond Films and Related Materials, edited by Y. Tzeng, M. Yoshikawa, M. Murakawa and A. Feldman, (1991), 489-94.

13. P. J. Fallon and L. M. Brown, Diamond and Related Materials, **2**, 1004-1011 (1993).

14. J. L. Kaae, P. K. Gantzel, J. Chin and W. P. West, J. Mater. Res., **5**, 1480-1489 (1990).

15. J. W. Edington, in *Practical Electron Microscopy In Materials Science* (Philips Company, The Netherlands, 1976), 109-205.

16. D. A. Smith and W. Krakow, Mat. Res. Soc. Symp. Proc., **83**, 349-353 (1987).

17. B. R. Stoner, C.-T. Kao, D. M. Malta and R. C. Glass, Applied Physics Letters, **62**, 2347 (1993).

Figure 1. SEM micrograph of a highly oriented {100} diamond film. Arrows indicate examples of misorientation between grains.

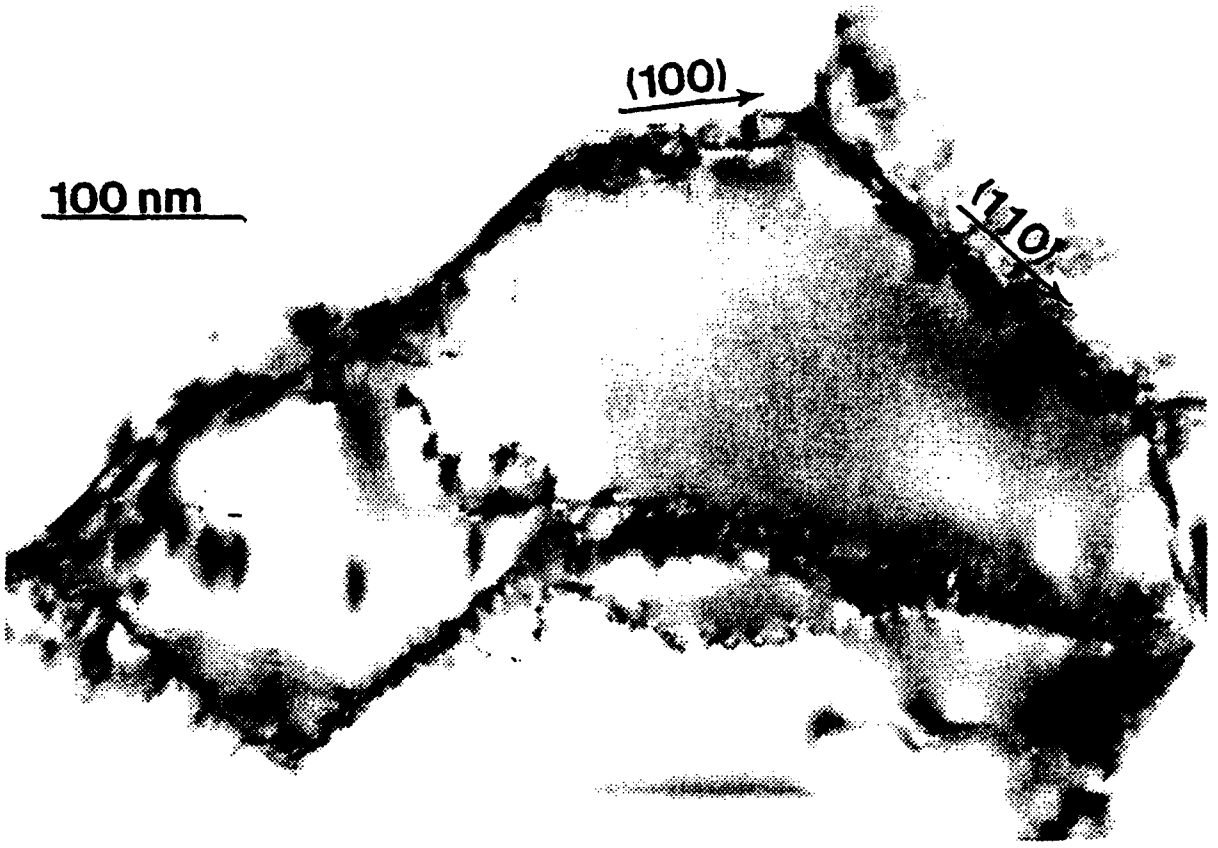

Figure 2. TEM micrograph showing defects at the grain boundaries. Boundaries parallel to both the <100> direction and <110> direction are present.

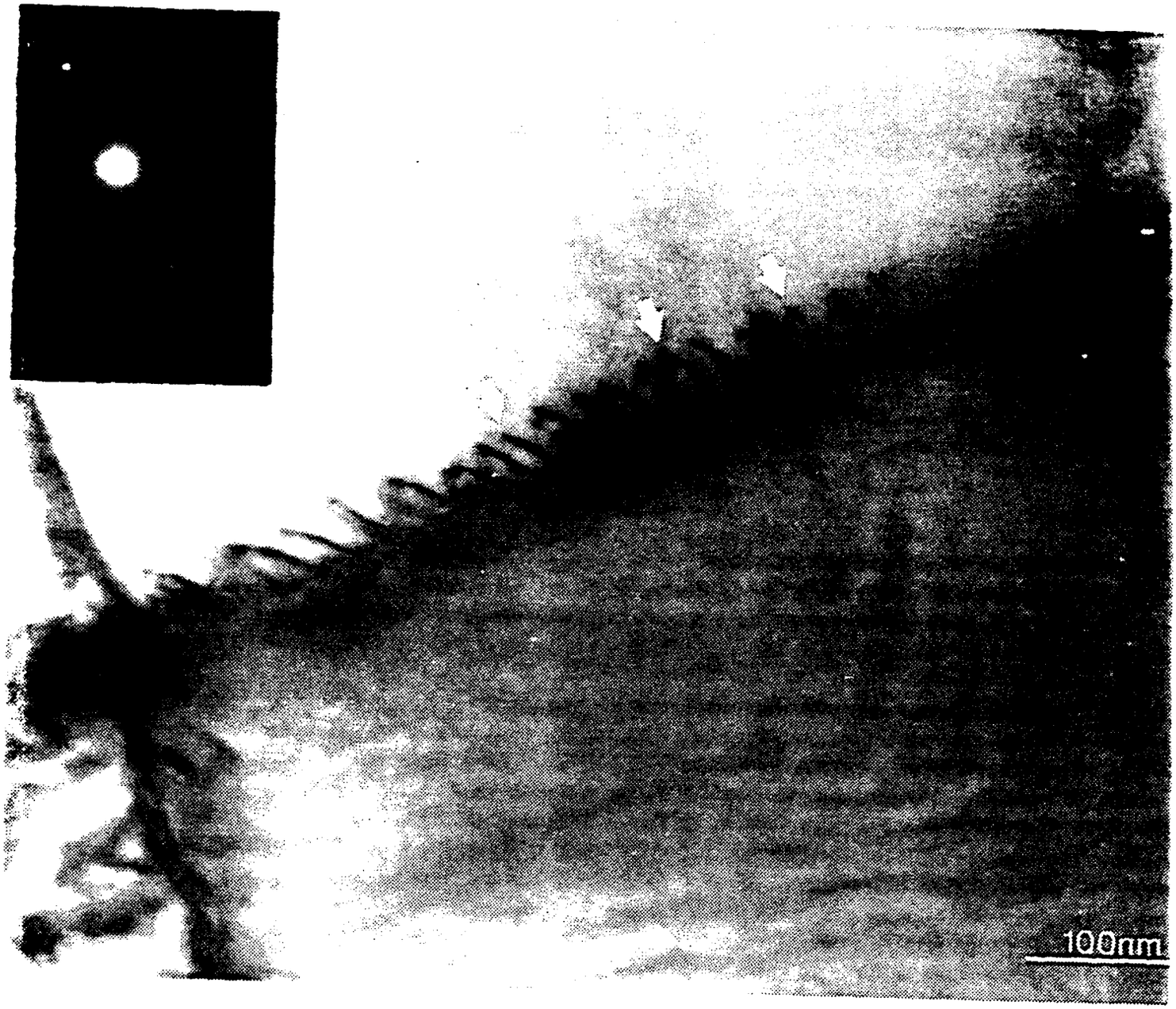

Figure 3. TEM micrograph showing widely spaced dislocations at the grain boundary. Arrows indicate every fifth dislocation where the spacing between each dislocation is approximately 20 nm. Inset shows a diffraction pattern from the grain boundary.

IV. Negative Electron Affinity Effects on the Diamond (100) Surface

J. van der Weide, Z. Zhang, P. K. Baumann, M. G. Wensell,

J. Bernholc and R. J. Nemanich

Department of Physics and Department of Materials Science and Engineering,

North Carolina State University,

Raleigh, North Carolina 27695-8202

Abstract

A negative electron affinity (NEA) was found both experimentally by photoemission spectroscopy and theoretically by *ab initio* calculations for the 2×1 reconstructed diamond (100) surface. This surface is the dominant growth surface for diamond thin films and can be obtained by chemical vapor deposition. Various surface preparation methods which result in a NEA are described. Theoretical results indicate that the observed NEA is associated with a monohydride terminated surface, while the hydrogen-free surface exhibits a positive electron affinity.

Submitted to Physical Review Letters, PACS numbers: 73.30.+y, 79.60.Eq, 81.60.Cp

Negative electron affinity (NEA) surfaces are semiconductor surfaces that have a work function such that the vacuum level lies below the conduction band edge. Electrons that are present in the conduction band can therefore readily escape the surface. The NEA surfaces are utilized in a number of important applications, such as photocathodes, secondary electron emitters, and cold-cathode emitters. In general, wide bandgap semiconductors are particularly suitable candidates for NEA emitters, since the conduction band minimum is likely to be close to the vacuum level. Diamond, which has a 5.5 eV bandgap, can be grown as high quality homoepitaxial and heteroepitaxial films with (100) oriented surfaces [1]. We have investigated the possibility of inducing a NEA on the diamond (100) surface and have found several surface preparation methods which led to this effect. *Ab initio* calculations were used to compute the electron affinity of different surface structures, and to identify the structure of the NEA surface and the origin of the NEA effect.

Photoemission is a highly sensitive tool to determine the presence of a NEA. Electrons that are excited in the photoemission process from the valence band into various conduction band energy levels lose energy through inelastic collision processes and accumulate in levels at the conduction band minimum. At a NEA surface, the vacuum level lies below the conduction band and the electrons accumulated at the conduction band minimum can be emitted into the vacuum. These electrons appear in the photoemission spectra as a sharp peak at low electron energies. The position of the peak can be correlated with other features in the photoemission spectra to verify that the emission originates from the conduction band minimum.

A NEA has been demonstrated for the diamond (111) surface [2] and has been associated with the presence of hydrogen bonded to the surface [3, 4]. The bulk terminated diamond (100) surface has two unsatisfied bonds which would in principle allow the formation of a dihydride terminated surface. The existence of the dihydride terminated surface has been subject to some debate [5-9]. Recent large scale *ab initio* calculations indicate that this surface is locally stable, but it is preferred only at very high values of hydrogen chemical potential [10]. It is, therefore, uncertain whether a stable dihydride terminated surface can be achieved. Diamond thin films, grown at 700-1000°C in a hydrogen rich environment, typically exhibit a 2×1 reconstruction. This surface is found to be stable in air [11], and is presumed to be a monohydride terminated surface [7]. A 2×1 reconstructed surface can also be obtained by annealing the diamond surface to ~1000°C. Temperature programmed desorption studies indicate that at these temperatures the monohydride evolves from the surface [7, 12], and it has been suggested that this surface is free of hydrogen [7].

In this study natural diamond wafers with a (100) surface orientation were polished with diamond grit, etched in chromic acid and *aqua regia* and introduced into the vacuum system. The wafers measured $3 \times 3 \times 0.5$ mm^3, and were type IIb (p-type semiconducting) with

resistivities of 10^3–10^4 Ωcm. Photoemission was excited with 21.21 eV light from a helium discharge lamp. The photoemission spectra, shown in Fig. 1, were obtained after the diamond surface had been annealed to temperatures ranging from 545°C to 1070°C. The spectra exhibited small, random shifts on the order of 0.2 eV with respect to each other. This is attributed to charging effects. The spectra were therefore aligned according to a bulk feature indicated by the line in Fig. 1 to allow comparison between them. As can be seen in the figure, the low energy onset of the spectra shifts by as much as 1 eV towards lower energies as the annealing temperature is increased. This is indicative of a lowering of the work function of the surface since electrons with lower energies are able to escape from the surface. After a 1035°C anneal the spectrum exhibits a peak at low energies which becomes more pronounced after a 1070°C anneal. As mentioned above, the appearance of this peak indicates that the vacuum level lies below the conduction band edge and that the surface has a NEA. The peak is positioned ~7.5 eV below the bulk feature indicated by the solid line in Fig. 1. An identical peak at ~7.5 eV below this bulk feature can be observed in the spectra of NEA diamond (111) surfaces [13–15]. The appearance of the peak on the (100) surface coincided with the appearance of a 2×1 surface reconstruction.

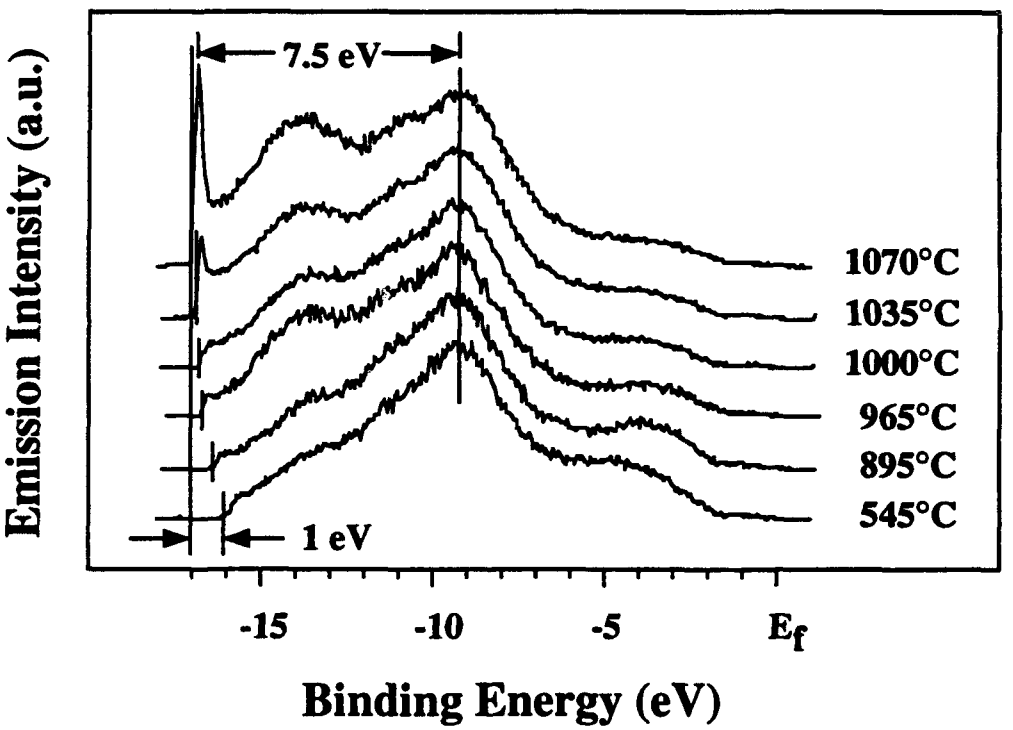

Figure 1. Photoemission spectra showing the effects of annealing on the diamond (100) surface. The shift in the back edge is indicative of a lowering of the work function and the presence of the sharp peak indicates a NEA. The spectra have been aligned according to the peak at ~9 eV below the Fermi level.

Auger electron spectra, shown in Fig. 2, indicate the presence of oxygen on the as-loaded surface which remained present after various anneals ranging from 500°C to 900°C. A reduction in the oxygen signature was observed after repeated anneals to 900°C. No oxygen could be detected after the diamond had been annealed to 1050°C. The surface was observed to transform from a 1×1 structure to a 2×1 structure, coincident with the removal of oxygen from the surface. The presence of hydrogen on the 1×1 and 2×1 surfaces cannot be determined from these measurements since AES is not sensitive to hydrogen. However, since no special efforts were made to obtain a strictly oxygen terminated surface, it is likely that hydrogen was also present on the surface.

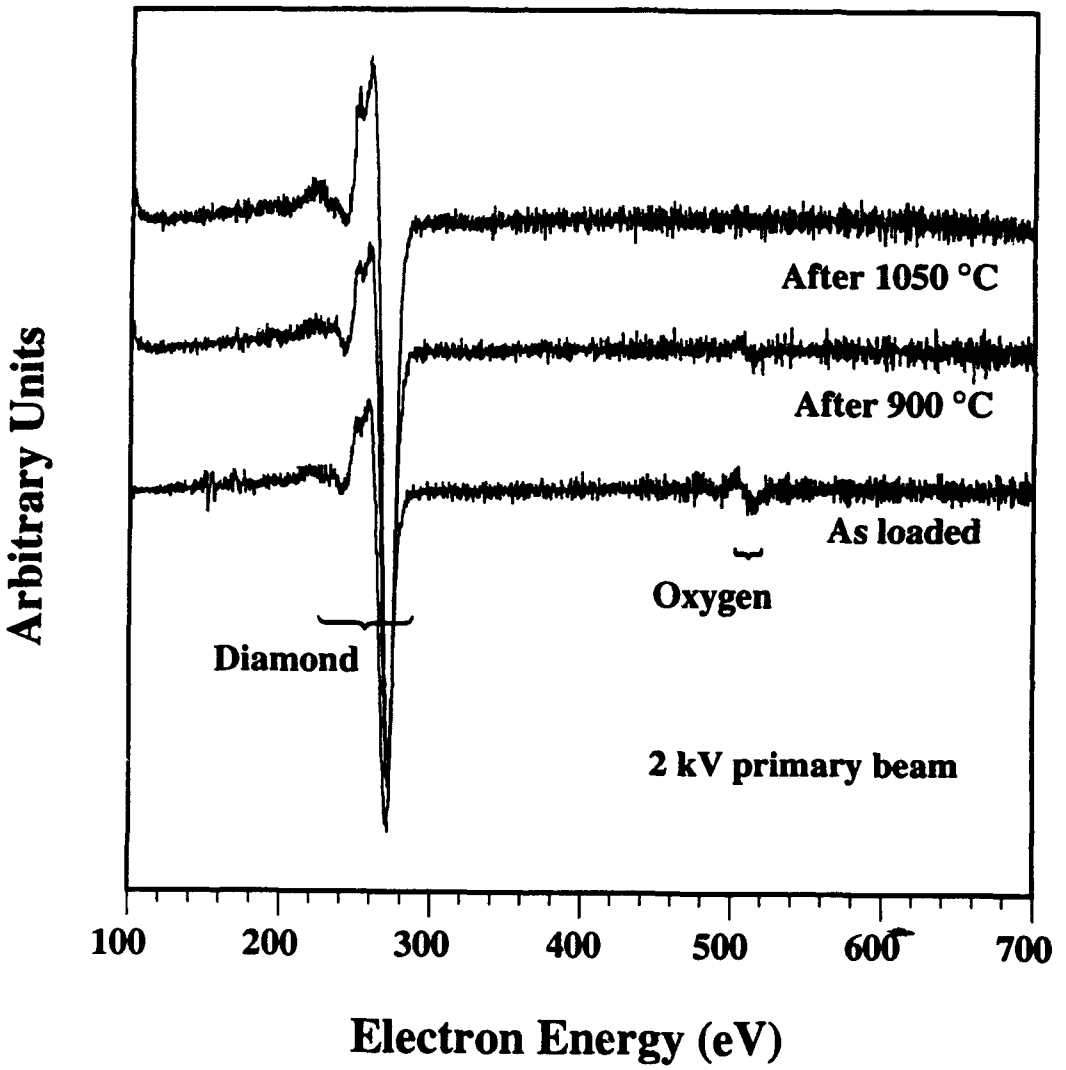

Figure 2. Auger spectra, obtained from the diamond (100) surface, as a function of annealing temperature. Oxygen, which is present on the surface after sample preparation, is observed to evolve at ~900°C, and removed after a 1050°C anneal. The removal of oxygen coincides with the transformation of the surface from a 1×1 to a 2×1 reconstructed surface.

Neither LEED nor AES can be used to determine whether the observed 2×1 reconstructed surface is a hydrogen-free or a monohydride terminated surface. In order to resolve that we have carried out *ab initio* calculations for both the bare and the hydrogen terminated 2×1 reconstructed diamond surfaces. The calculations were based on the Local Density Approximation (LDA) and the Car-Parrinello formalism [16]. The hydrogen-free (100) surface was modeled by a supercell consisting of a slab of ten layers of diamond with twelve carbon atoms on each layer. The slabs were separated by 10 Å of vacuum. One hydrogen atom was attached to every surface carbon atom to model the monohydride surface. Due to the size of the supercell, only Γ point sampling was used. Starting from an approximate structure, the ground state geometry was obtained by steepest descents and/or fast relaxation methods [17]. The vacuum level of the surface was determined from the plane-averaged, self-consistent potential in the vacuum region. Since calculations based on the local density approximation do not reproduce well the experimentally measured bandgap [18], the position of the conduction band minimum is determined by adding the experimental value for the bandgap (5.47 eV) to the position of the valence band maximum. The position of the valence band maximum was found by adding the energy difference between the average self-consistent potential in the bulk and the highest occupied energy level in bulk calculations to the average self-consistent potential inside the slab.

The calculations indicated that the monohydride terminated surface relaxes to a 2×1 reconstructed surface. The plane-averaged, self-consistent potential for this surface is shown as a function of the distance to the surface in Fig. 3. As can be seen in the figure, the effective potential has flattened out in the vacuum region, which indicates that the slab separation used in the calculations is sufficiently large to avoid interactions between the slabs. The flat region is representative of the vacuum level. The conduction band minimum is found at ~2.2 eV above the vacuum level, resulting in a ~2.2 eV NEA for C(100)-2×1:H surface.

The bare C(100) surface also relaxes to a 2x1 reconstruction, with a geometry similar to that obtained by other authors [9, 19]. Substantial displacements from the ideal bulk positions were found in the surface layers. The plane-averaged self-consistent potential for this surface is also shown in Fig 3. A ~0.8 eV positive electron affinity was found for this surface. We also find that occupied surface states exist inside the bandgap near the valence band maximum, in agreement with photoemission studies [20]. The calculations indicate that these states are related to dangling bond orbitals on the dimer atoms. The electronic charge in these dangling orbitals results in a stronger dipole layer of the bare surface when compared to the hydrogenated surface. The differences in work function and electron affinities between these two surfaces are due to this dipole layer.

The CVD grown diamond (100) surface is known to exhibit a 2×1 reconstruction, which has been shown to be stable in air [11]. This 2×1 reconstruction has been attributed to the

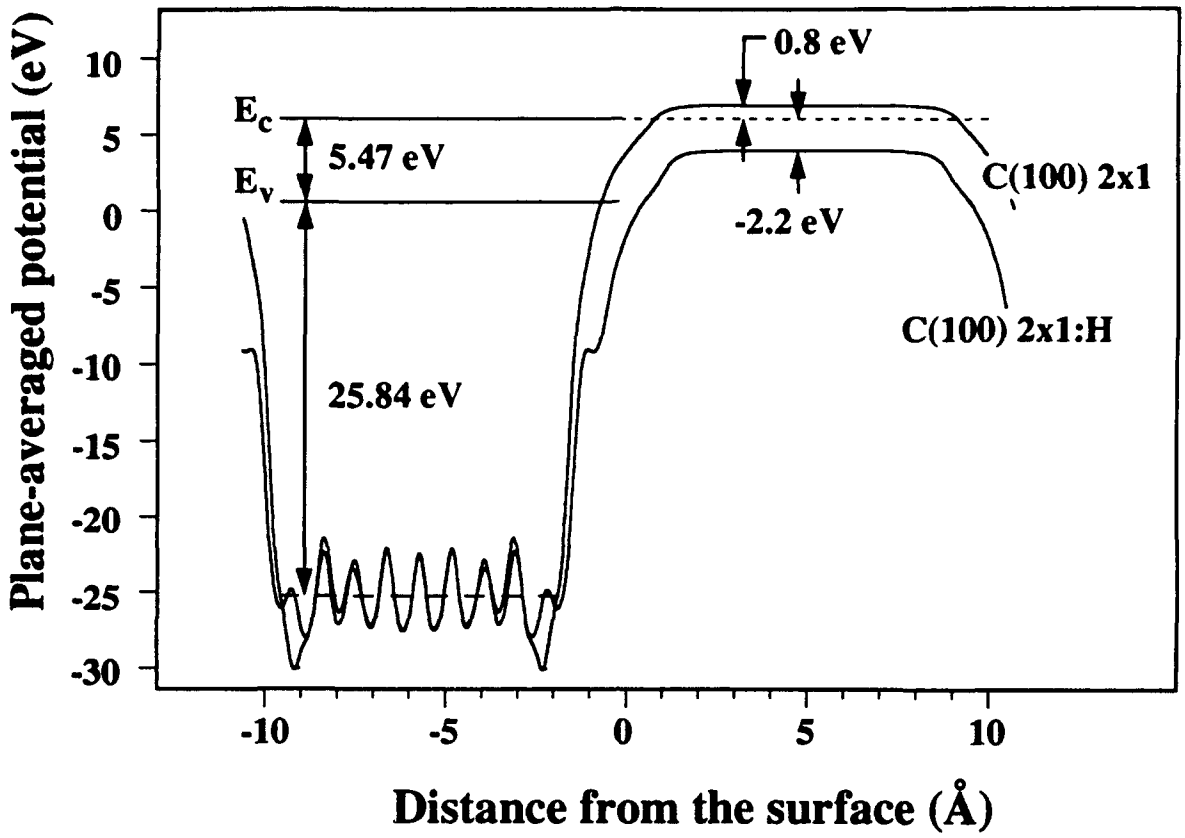

Figure 3. Calculated plane-averaged, self-consistent potentials of a hydrogen-free and monohydride terminated 2×1 reconstructed diamond (100) surface.

presence of a monohydride structure [5–7]. Based on the results described above it is expected that the CVD growth surface would exhibit a NEA. Diamond was deposited on a (100) oriented, type IIb wafer, resulting in a homoepitaxial film. After transport in air a faint pattern associated with the 2×1 reconstruction could be discerned. The film was etched to remove a dark discoloration which was due to the deposition process. After the etch, the 2×1 reconstruction could not be discerned but the 1×1 bulk pattern remained. Photoemission spectra, shown in Fig. 4, exhibited a clear peak at 7.3 eV below the bulk feature indicating the presence of a NEA. This result suggests that the (100) oriented growth surface exhibits a NEA which is unaffected by exposure to air and various etches.

Typical diamond growth conditions consist of surface temperatures ranging from 700°C to 1000°C and exposure to a hydrogen plasma with a small (< 5%) amount of a carbon containing gas mixed in. To emulate growth conditions, natural diamond wafers were exposed to a pure hydrogen plasma while heated to 350°C and 500°C. It was found that under these conditions a NEA could be induced as well. This result supports the conclusion that the growth surface exhibits a NEA which is related to hydrogen termination.

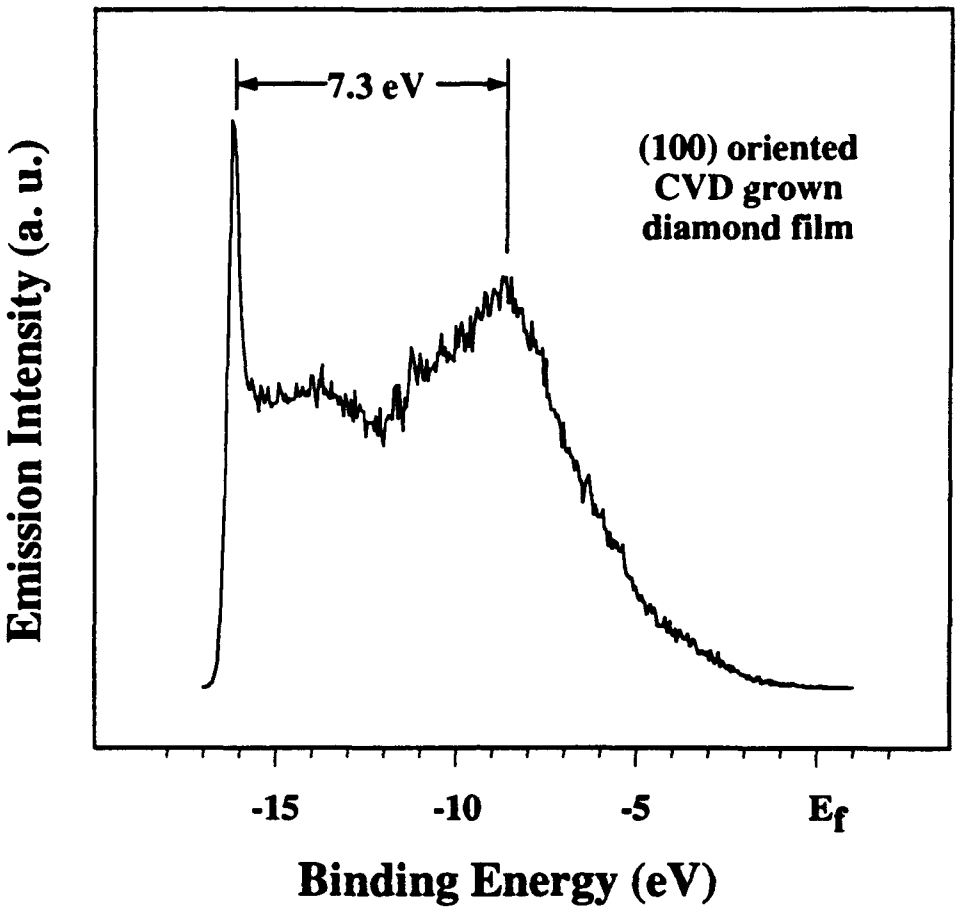

Figure 4. Photoemission obtained from a CVD grown, (100) oriented diamond film indicates the presence of a NEA.

In summary, a NEA was obtained on the diamond (100) by annealing a polished and chemically cleaned surface to ~1000°C. This resulted in the desorption of oxygen and the appearance of a 2×1 reconstruction. Theoretical calculations indicate that the NEA is associated with a monohydride terminated surface. It was found that CVD-grown diamond film, which results in a similar surface structure, exhibits a NEA. A NEA can also be induced by exposing a surface heated to 350-500°C to a hydrogen plasma, supporting the conclusion that the growth surface exhibits a NEA. Many more NEA emitters are likely to be found as the methods for growth of wide bandgap semiconductors are improved. Local-density-based calculations, when corrected for bandgap effect, appear to predict correctly the occurrence of the NEA effect. These calculations can thus be used to identify other promising passivant-semiconductor combinations for NEA emitters, and to establish trends in dipole strength and sign. Photoemission experiments provide unambiguous evidence of the existence of NEA, and can be used both to calibrate the theoretical findings and to verify the actual occurrence of NEA.

The authors would like to acknowledge L.S. Plano and K. Das of Kobe Research for diamond film growth and polishing. This work was supported in part by the Office of Naval Research through grants N0014-92-J-1477 and N0014-92-J-1604 and the National Science Foundation through grants DMR-9204285 and DMR-9100063.

References

1. S. D. Wolter, B. R. Stoner, J. T. Glass, P. J. Ellis, D. S. Buhaenko, C. E. Jenkins and P. Southworth, Appl. Phys. Lett. **62**, 1215 (1993).
2. F.J . Himpsel, J. A. Knapp, J. A. van Vechten and D. E. Eastman, Phys. Rev. B **20**, 624 (1979).
3. B. B. Pate, Surf. Sci. **165**, 83 (1986).
4. B. B. Pate, M.H. Hecht, C. Binns, I. Lindau and W.E. Spicer, J. Vac. Sci. Technol. **21**, 364 (1982).
5. Y. L. Yang and M. P. D'Evelyn, J. Vac. Sci. Technol., A. **10**, 978 (1992).
6. Y. L. Yang and M. P. D'Evelyn, J. Am. Chem. Soc. **114**, 2796 (1992).
7. Y. L. Yang, L. M. Struck, L. F. Sutcu and M. P. D'Evelyn, Thin Solid Films **225**, 203 (1993).
8. B. N. Davidson and W. E. Pickett, preprint
9. S. H. Yang, D. Drabold and J. B. Adams, Phys. Rev. B **48**, 5261 (1993).
10. M. G. Wensell, Z. Zhang and J. Bernholc, to be published.
11. T. Tsuno, T. Imai and Y. Nishibayashi, Jap. J. Appl. Phys. **30**, 1063 (1991).
12. R. E. Thomas, R. A. Rudder and R. J. Markunas, J. Vac. Sci. Technol. A **10**, 2451 (1992).
13. J. van der Weide and R. J. Nemanich, submitted to J. Appl. Phys.
14. J. van der Weide and R. J. Nemanich, J. Vac. Sci. Technol. B **10**, 1940 (1992).
15. J. van der Weide and R. J. Nemanich, Appl. Phys. Lett. **62**, 1878 (1993).
16. R. Car and M. Parrinello, Phys. Rev. Lett. **55**, 2471 (1985).
17. C. Wang, Q.-M. Zhang and J. Bernholc, Phys. Rev. Lett. **69**, 3798 (1992).
18. D. Hamman, M. Schluter and C. Chiang, Phys. Rev. Lett. **43**, 1494 (1979).
19. S. P. Mehandru and A. B. Anderson, Surf. Sci. **248**, 369 (1991).
20. A. V. Hamza, G. D. Kubiak and R. H. Stulen, Surf. Sci. **237**, 1 (1990).

V. The Origin of the Broadband Luminescence and the Effect of Nitrogen Doping on the Optical Properties of Diamond Films

A. Introduction

A broadband luminescence extending from approximately 1.5 to 2.5 eV and centered at ~ 2 eV has been observed in various photoluminescence (PL) studies of diamond films grown by the chemical vapor deposition (CVD) method [1–5]. This broadband PL appears as the strongest feature in the spectrum. However, a complete model has yet to be formulated to explain the origin of this broadband PL. Studies utilizing cathodoluminescence and absorption spectroscopy of crystal diamonds of types 1a and 1b which contain nitrogen have shown that similar broadband luminescence has its origin in the electron-lattice coupling (vibronic interaction) of nitrogen related centers with zero phonon lines at 1.945 and 2.154 eV [6–7]. These centers, when optically excited, can interact with the lattice vibrations via various mechanisms. One type of electron-lattice interaction is energy-transfer from a photo-excited optical center to the phonons which results in a broadband PL spectra. The broadband PL in this case will extend toward lower energy relative to the zero phonon line. Luminescence studies on natural brown diamonds [8-9] have shown that the brown diamonds luminesce in the yellow and in the red region of the spectrum. The luminescence appears in the optical spectra as wide bands centered at ~ 2.2 eV and at ~ 1.8 eV. The spectral width of these luminescence features are again very similar to the one observed in the spectra of the CVD diamond films. The origin of the wide luminescence bands of the brown diamonds has also been determined to be of vibronic nature. In this report we investigate the origin of the broadband luminescence in CVD diamond films, exclude the possibility of the broadband PL originating from any vibronic interaction, and posit a different mechanism of origin.

An alternative mechanism which could give rise to the broad PL band in the CVD diamond films is the amorphic phase of the sp^2-bonded carbon (also called the graphitic phase), the presence of which has been widely confirmed [10–12]. The PL of amorphous carbon films exhibit emission centered at ~ 1.8–2 eV which is of similar line shape to that observed in the CVD diamond films [13–17]. According to the general model of the state distribution of amorphous materials [18–19], the distortions of bond angles and of bond lengths which constitute the amorphous phase introduce a continuos state distribution in the optical band gap of the material. The PL of amorphous carbon films has been determined to originate in the optical transitions of an in-gap state-distribution related to the disordered forms of the sp^2 carbon bonding. In this report we establish the presence of an in-gap state-distribution in CVD diamond films and suggest that it is the likely cause of the broadband luminescence. It is crucial to electro-optic applications to have knowledge of the properties of this distribution since it can affect and determine the transport and recombination mechanisms of the carriers.

The first part of this report presents the results of detailed PL studies of nitrogen-doped CVD diamond films. We identify the nitrogen PL centers most likely to be created in the films: the 1.945 eV, 2.154 eV, the band-A and a possible new nitrogen center at 1.967 eV. We show that the broad PL band does not originate from the vibronic interaction of the nitrogen related centers at 2.154 eV and 1.945 eV. Furthermore, it is shown that the temperature dependence of the broad PL band does not obey the empirical relation expected from electron-lattice interactions. The integrated intensity of a vibronic broadband is expected to increase with increasing temperature since the electron-phonon coupling becomes more probable [20]. We found, however, that the intensity decreases with increasing temperature. We therefore exclude the possibility of the broadband PL being of vibronic origin.

In the second part of this paper we establish that the broad PL band in the CVD diamond films has characteristics of an optical emission originating from a continuous distribution of in-gap states very similar to that found in amorphous materials. From correlation of the sp^2 amorphous phase present in the diamond film to the PL emission we conclude that the sp^2 amorphous phase introduces an in-gap state distribution which initiates the broadband PL. We also present the results of an investigation into the main properties of the state distribution: its profile, density and width. These parameters are important because the density of states is a measure of the amount of the amorphic phase present in the material, while the width reflects the magnitude of the fluctuation in the distortion of bond length and angle. Our experimental results are analyzed in terms of the model of in-gap state distribution for amorphous materials developed by Street et al. [19, 21–22]. Our PL experimental data indicate that the profile of the state distribution is of an exponential form whose specific shape depends on the exact growth conditions.

B. Experiment

In this study diamond samples were grown on Si (100) substrates using an ASTeX microwave plasma CVD system. The plasma power, temperature and pressure were maintained at 900 watts, 850°C and 25 Torr respectively. Three samples involved in the nitrogen study were subjected to H_2 / CH_4 / N_2 flow rates of 500 / 5 / 0, 500 / 5 / 0.5 and 500 / 5 / 10 sccm and will be referred to as the 0%, 0.1% and 2% nitrogen-doped samples, respectively, according to their gas phase N_2/H_2%. The growth time for these samples was 5 hours.

The two undoped diamond samples involved in the density of state distribution investigation were used in our previous study [23] and will be referred to as the 20h and the 40h samples, reflecting their respective growth times. Both samples are continuous, with the 20h sample being about 2 μm thick and the 40h sample being about 4 μm thick. The plasma

for the 20h and the 40h samples consisted of 1% CH_4 in H_2 at 1000 sccm total flow. The plasma power, chamber pressure and substrate temperature were maintained at 800 watts, 25 Torr and 750°C, respectively. The scanning electron microscope (SEM) micrographs of the above samples are shown in Fig. 1.

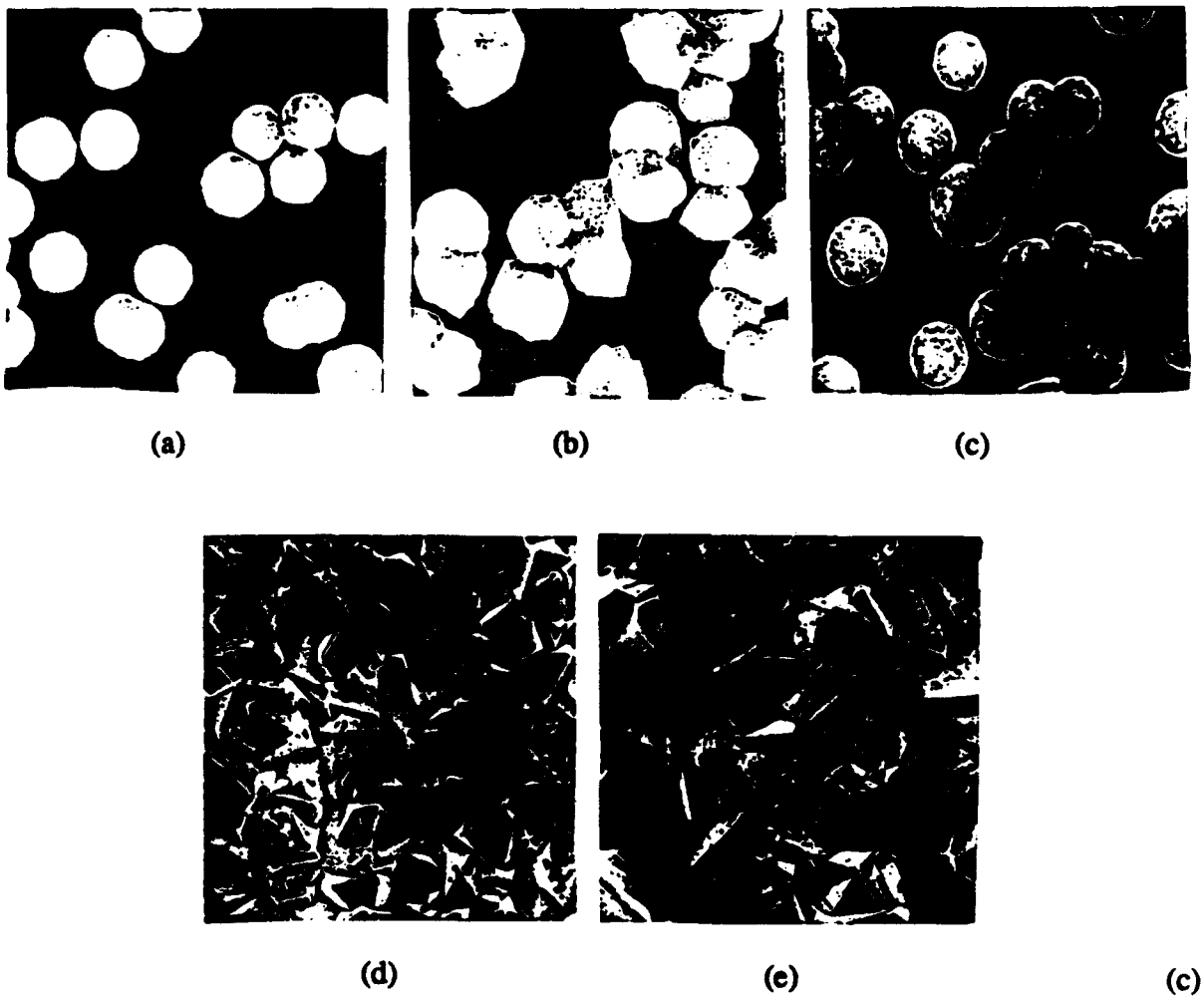

Figure 1. The SEM micrographs of (a) 0%, (b) 0.1%, (c) 2% nitrogen doped samples and of the (d) 20h, (e) 40h undoped samples.

The micro-PL and Raman analysis of the 0%, 0.1% and 2% nitrogen-doped samples was carried out at room temperature employing Argon-ion laser excitation (514.5 or 457.9 nm) which was focused on the sample to a spot of ~ 5 μm in diameter. Focusing was facilitated by using an Olympus BH-2 microscope. The macro PL analysis of the 20h and the 40h samples was carried out employing a JANIS CCS-350 closed cycle refrigerator system. The spot size of the laser line was ~ 2 mm × 100 μm. In both studies, an ISA U-1000 scanning double monochrometer was used to analyze the signal.

C. Results and Discussion

PL and Raman Line Shape Investigation. The first part of our work focused on obtaining the PL spectra of nitrogen-doped and undoped diamond films, identifying the nitrogen-related PL bands and examining the influence of the nitrogen on the broadband PL. In Fig. 2 the PL spectra of the 0.1% N-doped and undoped diamond films are shown. Both spectra were obtained utilizing the 514.5 nm green line of the Argon laser. The PL spectra of the undoped diamond film exhibits the fairly smooth broadband line shape centered at ~ 2.05 eV, and also exhibits the 1.68 eV band which has been attributed to an optical transition in a Si complex center [10, 24–27]. However, the spectra of the N-doped film indicates a red-shift of the broadband luminescence center as well as a line-shape change. Furthermore, the nitrogen-related bands at 2.154 and 1.945 eV are present. Studies carried out by Davies *et al.* [7] have suggested that the 1.945 eV band is due to the substitutional nitrogen-vacancy optical center. Collins *et al.* [6] proposed that the 2.154 eV band is the result of a transition in a center consisting of a single substitutional nitrogen atom with one or more vacancies. Yet another PL band at 1.967 eV is also present in the spectra (barely distinguishable from the 1.945 eV band), which might also be due to a nitrogen-related center. The possibility that the 1.967 eV band is nitrogen-related will be the subject of future investigation.

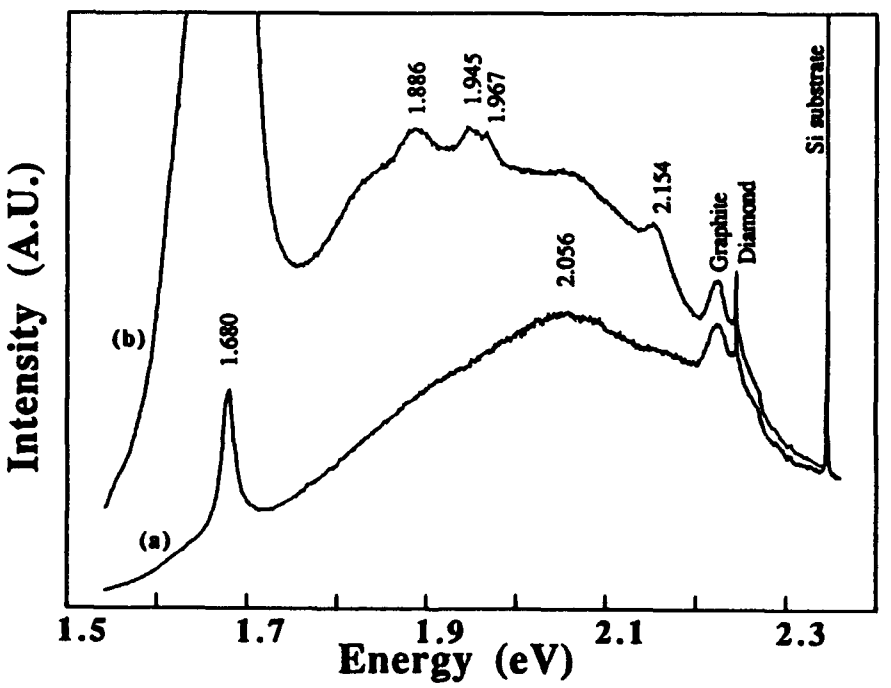

Figure 2. The PL spectra of (a) 0% nitrogen sample and (b) of 0.1% nitrogen doped sample employing the 514.5 nm laser line. Raman bands are labeled as to origin and the peak energy of the PL bands are indicated.

In order to examine in further detail the line-shape of the broadband luminescence, the 457.9 nm blue laser line was used for excitation. Figure 3 shows the spectra of the undoped and of the N-doped diamond films for this laser frequency. The broadband luminescence of the undoped diamond film retained its relatively unstructured line-shape; however, the maximum intensity is shifted towards higher energy and is centered at ~ 2.2 eV. The spectra of the nitrogen-doped diamond film exhibits the nitrogen-related band at 2.154 eV, as well as the 1.967 eV band. The 1.945 eV band, which appeared with the 1.967 eV band as a doublet in the spectra obtained using the green laser line, can not be clearly distinguished in the spectra taken using the blue line. This overlapping of the two bands is a resolution artifact of the scaling of the spectra using the blue laser line. A relatively wide band with line-width ~ 0.3 eV centered at 2.46 eV is also present. Similar wide-band luminescence has been observed in both natural and synthetic diamonds [28-30], and is commonly referred to as "band A" luminescence. This band has variable peak energy and line-width depending on the concentration of the nitrogen in the diamond. The band A luminescence has been suggested to originate from aggregates of nitrogen which consist of a nearest-neighbor pair of nitrogen atoms [30]. The presence of the aggregate form of nitrogen in the CVD diamond films and in diamond grown by the combustion flame method has also been reported for cathodoluminescence measurements [31-33]. It was there shown that the band A centers may

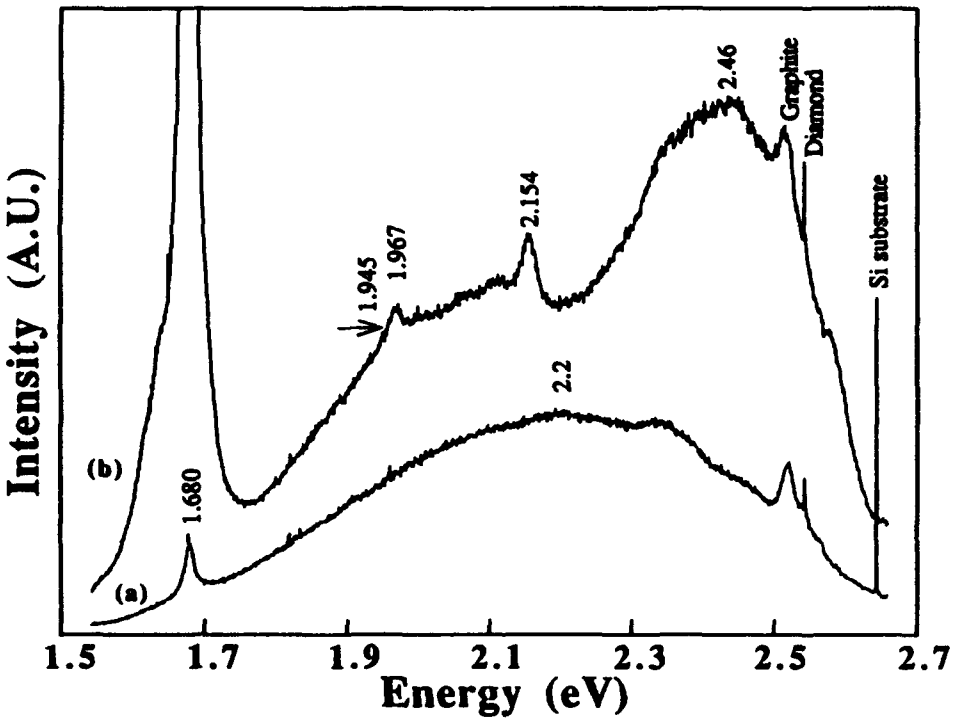

Figure 3. The PL spectra of (a) 0% nitrogen sample and (b) of 0.1% nitrogen doped sample employing the 457.9 nm laser line.

be localized at dislocation-type defects in the CVD diamond. Our observation of the three nitrogen-related bands in the spectra may indicate that the paramagnetic (1.945, 2.154 eV) as well as the non-paramagnetic (band A) forms of nitrogen centers can exist simultaneously in the CVD diamond films. It is also evident from the spectra that the incorporation of nitrogen caused a distortion in the line-shape of the underlying broadband luminescence. If the broadband PL had been due to the nitrogen-lattice interaction, the line-shape would have been invariant, and a change in the intensity would have been anticipated.

A second series of experiments and analysis were conducted to further rule out the possibility of the broadband luminescence being of vibronic origin. According to the theoretical model of the electron-lattice interaction [20, 34], the total band intensity which includes the zero-phonon line and its vibronic sideband is expected to be independent of temperature. As the temperature increases the zero-phonon line relative intensity decreases, and the vibronic band relative intensity is expected to increase as:

$$I \sim \coth\left(\hbar\omega / 2k_B T\right) \tag{1}$$

so as to keep the total intensity constant with temperature [20]. The width of the vibronic band is also expected to increase with temperature as the square-root of Eq. (1). In this relation ω is the central frequency of the vibronic band and k_B is the Boltzmann constant. Eq. (1) depicts the effect of the interaction between the thermal vibrations of the lattice and the optical centers on the PL vibronic band. According to this formulation, as the temperature increases more phonons are created in the material and are available to interact with the optical center transitions: this interaction should appear as a vibronic band in the PL spectra. However, as shown in Fig. 4 we found instead that the broadband PL intensity exhibits a relatively rapid decrease with increasing temperature without any change in the band width. This temperature dependence which is not characteristic of a vibronic interaction will be discussed in further detail in the next section of this paper; it will be shown that a non-radiative channel caused by a density of gap-states competes with the PL process and quenches the broadband luminescence.

The results of the first and second experiments suggest that the broadband PL in diamond films is not due to the nitrogen-lattice interaction system, nor is it of other vibronic origins. The incorporation of nitrogen instead manifests itself in a change in the PL line-shape toward the lower energy side resulting from the electron-phonon coupling in the 2.154 and in the 1.954 eV nitrogen centers.

We now present the preliminary results of the effects of nitrogen-doping on the diamond quality. The Raman spectra of the 0, 0.1 and 2% nitrogen-doped diamond films are shown in Figure 5. The spectrum of the 0.1% nitrogen-doped film indicates that this film has the better

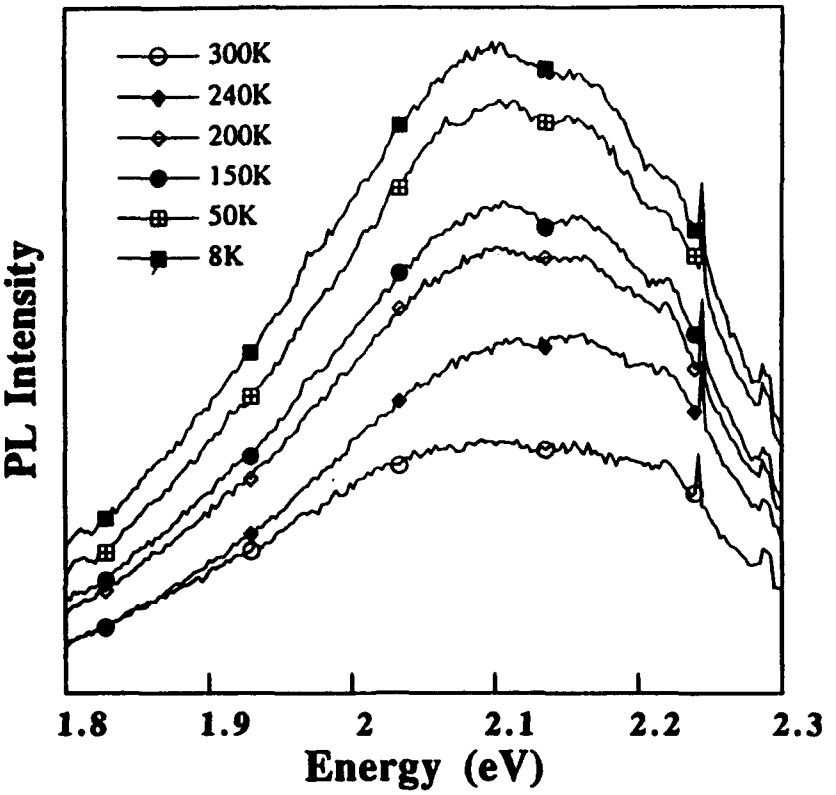

Figure 4. The spectra of the broadband PL of the 20h sample at various temperatures.

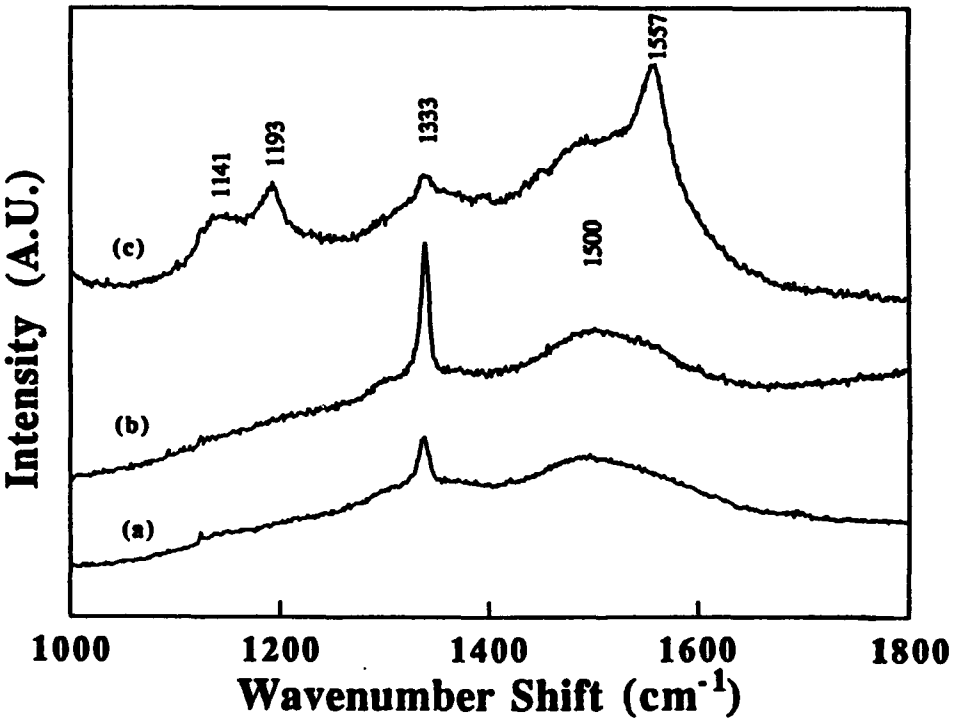

Figure 5. The Raman spectra of (a) 0% (b) 0.1% (c) 2% nitrogen doped samples.

quality diamond: the graphitic-to-diamond ratio (I_G/I_D) was found to be 4.6 whereas for the 0% nitrogen-doped film the graphitic-to-diamond ratio was 9.3. The spectrum of the 2% nitrogen-doped film indicates that a degradation of the diamond structure occurs at that relatively high nitrogen doping. It appears also that the graphitic phase of the 2% nitrogen-doped film exhibits an additional bonding type at 1557 cm^{-1}. Other Raman lines are also present at 1141 and 1193 cm^{-1} which we speculate to be due to bonding between nitrogen and carbon. We also note that the presence of nitrogen in the diamond film enhances significantly the 1.68 eV PL band. More detailed work will be carried out to investigate the nitrogen-effect on the quality of the CVD diamond films.

Characterization of the Broadband PL. Figure 6 shows the correlation between the Raman intensity of the graphitic phase and the intensity of the broadband PL. This correlation was found and described in detail in a previous study [23]. In that study, a film was grown in

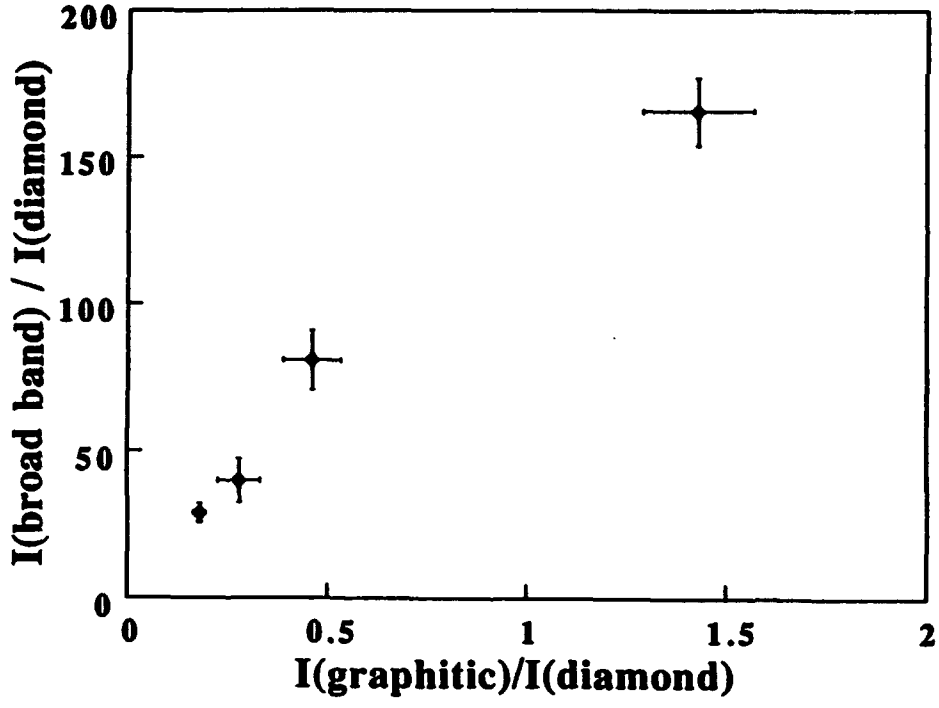

Figure 6. Correlation between the broadband PL intensity and the graphitic Raman intensity.

a series of stop-growths until it constituted a continuous film 4 μm thick. At regular time intervals the growth sequence was interrupted and the film was characterized. It was found that, as a function of growth time, as the graphitic phase increases as does the intensity of the broadband PL. We have suggested that the amorphic graphitic phase introduces a state distribution in the band gap which provides transition centers for the photo-excited carriers,

thus resulting in the broadband PL. We now present the results of a further investigation of the broadband PL obtained from the 20 h and the 40 h undoped diamond films. We establish that it has PL characteristics similar to those found in amorphous materials.

In general the PL efficiency η_{PL} can be expressed by the following equation [35]:

$$\eta_{PL} = \left(\frac{I}{I_0}\right) = \frac{P_R}{(P_R + P_{NR})} \tag{2}$$

where P_R and P_{NR} are the probabilities for the radiative and the nonradiative recombination respectively, I is the PL intensity, and I_0 is the PL intensity for the temperature approaching absolute zero. If there exists a single activation energy E_a for P_{NR} for which the thermal quenching of the luminescence is of the form of a Boltzmann activated process:

$$\exp\left(-E_a/k_BT\right),$$

and P_R is sensibly independent of temperature then Eq. (2) becomes

$$\frac{P_{NR}}{P_R} = \frac{I_0}{I(T)} - 1 \sim \exp\left(-E_a/k_BT\right) \tag{3}$$

By plotting

$$\log\left(\frac{I_0}{I(T)} - 1\right) \text{ vs. } 1/T,$$

a straight line should be obtained from which E_a can be evaluated. The experimental data presented in Figures 7 and 8, however, indicate the existence of a continuous distribution of activation energies E(T) rather than a single E_a associated with one energy level of a specific defect. Such a continuous distribution of activation energies E(T) indicates in turn a corresponding distribution of localized energy states in the band gap of the CVD diamond film. E(T) may thus be viewed as corresponding to the binding energies of these localized states. The data in Figures 7 and 8 can be fitted by the equation

$$\frac{I_0}{I(T)} - 1 \sim \exp\left(T/T_0\right) \tag{4}$$

Figure 9 shows the plot of

$$\log\left(\frac{I_0}{I(T)} - 1\right) \text{ vs. } T$$

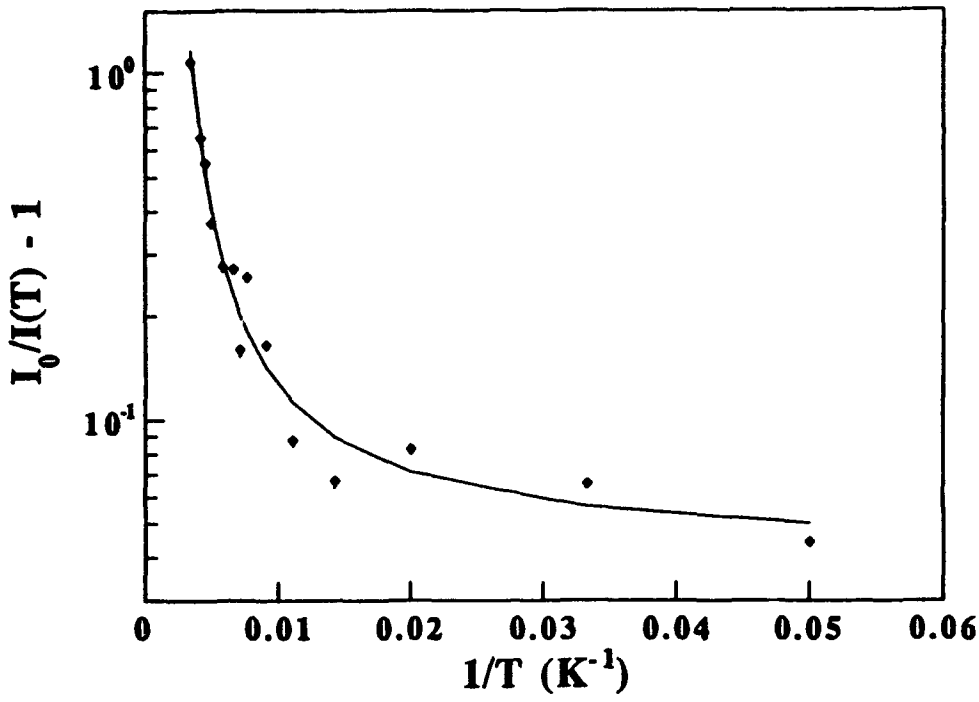

Figure 7. The functional behavior of the broadband PL vs 1/T as obtained from the 20h sample.

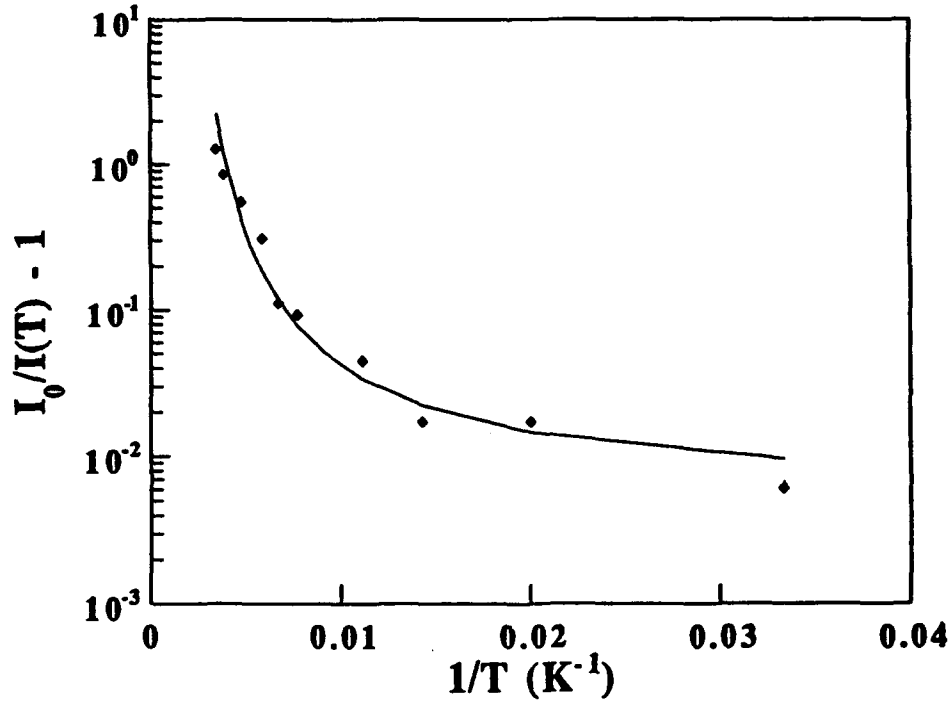

Figure 8. The functional behavior of the broadband PL vs 1/T as obtained from the 40h sample.

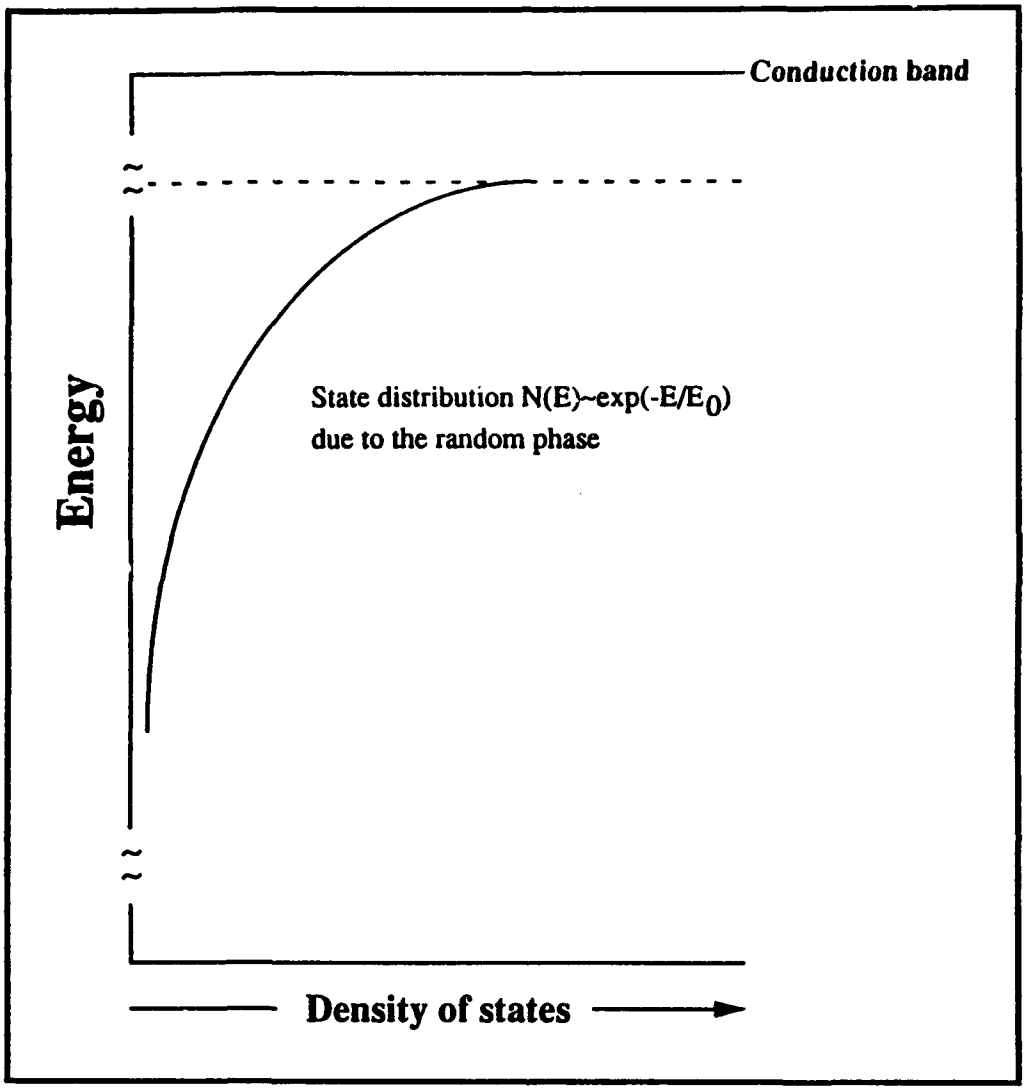

Figure 10. Density of state distribution of a general model of amorphous material.

measurements which at present are beyond our current capabilities. However, by inferring the value of $\omega_0\tau_R$ (as described in the following paragraph) and determining T_0, the latter which may be found from plots of the type presented in Figure 9, E_0's for both samples can be compared.

From the data presented in Figure 9, we have calculated T_0 to be ~ 85K for the 20h sample and T_0 to be ~50K for the 40h sample. This is in contrast to T_0 ~ 23K reported for hydrogenated amorphous Silicon [21]. Using these values of T_0 we may infer E_0 and the corresponding in-gap state distribution width by the following reasoning. It can be argued that the term $\ln(\omega_0\tau_R)$ in Eq. (6) has relatively small variation for different samples made of the same material. The escape frequency ω_0 in general depends upon the cross-section of the

bond types involved in the optical transition. Since for both of our samples the same type of bonding, sp^2, has been assumed to initiate the PL, ω_0 may safely be assumed to have the same value for the 20h and the 40h sample. The radiative decay time τ_R, on the other hand, has larger variation depending on the characteristics of the state distribution. Since the product $\omega_0\tau_R$ is the argument of a logarithmic function which is slowly varying, the value of $\ln(\omega_0\tau_R)$ may assume approximately the same value for both of our samples. In light of the above discussion, we may conclude that the in-gap state distribution of the 20h sample (T_0 = 85K) extends more widely into the band gap than the state distribution of the 40 sample (T_0 = 50K). The above finding may imply that the 20h sample exhibits greater variations in the sp^2 bond length than the 40h sample.

Further information concerning the density of the state distribution may be obtained from the dependence of the PL on the excitation intensity. The general relation between the PL intensity I_{PL} and the incident excitation intensity I_{EX} is of the form

$$I_{PL} \propto I_{EX}^{\alpha} \tag{7}$$

where the value of the constant α depends on intrinsic properties of the material which influence the luminescence. In the ideal case, $\alpha \sim 1$ indicating that the PL is due to recombination of an electron-hole pair created by the same photon. Figure 11 shows the plot of the broadband integrated luminescence vs. the excitation intensity power for the two

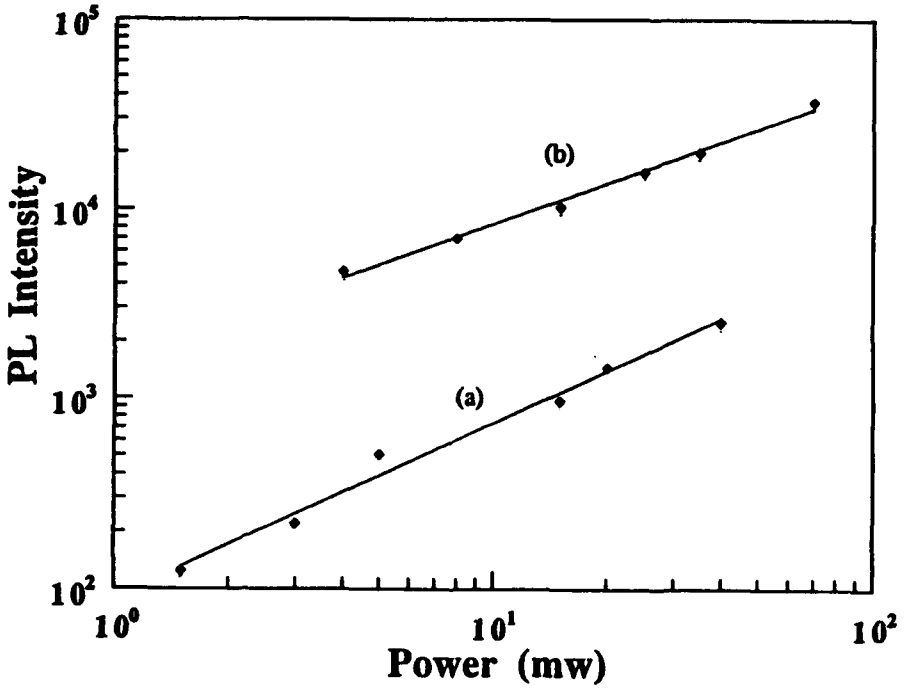

Figure 11. The broadband PL intensity vs the laser incident power of (a) the 20h and (b) the 40h sample. Data was obtained at T=10 K.

samples at 10K. For the 20h sample $\alpha \sim 1$ and for the 40h sample $\alpha \sim 0.8$. The deviation of α from unity may be qualitatively interpreted as being due to a non-radiative tunneling effect: if the density of the states is relatively high then the photo-excited carriers have a higher probability of tunneling to available neighboring states rather than following radiative recombination. The other possible mechanism which may affect the linearity of the PL is the energy transfer among the photo-excited carriers (Auger process); for a relatively low density of state and hence a relatively small concentration of photo-excited carriers, the probability of this process occuring is small. However, when the density of state is sufficiently high so as to generate a higher concentration photo-excited carriers, the probability of an Auger process is high and it may compete with the PL recombination process.

To support the above finding of different exponents, the ratios of the graphitic to the diamond Raman lines I_G/I_D were calculated for both samples. It was found that $I_G/I_D = 0.7$ for the 20h sample and $I_G/I_D = 1.7$ for the 40h sample. The higher concentration of the sp^2 phase in the 40h sample may explain the relatively high density of states which was predicted from the power-excitation experiment.

More extensive experiments need to be carried out to further quantify and model the state distribution and to determine the bands involved in the optical transitions. In amorphous carbon material the sp^2 bonding creates sigma-bands (σ, σ^*) and pi-bands (π, π^*) [13] for which optical transitions can occur. At present we hypothesize that the π-π^* band transitions are responsible for the broadband PL. The basis of this hypothesis lies on the knowledge that the allowable optical transitions in crystalline graphite [36] are the π-π^*, σ-σ^* and the σ-π^* for which only the π-π^* bands lie in the energy range closest to our laser excitation energy.

Our initial investigation suggests the existence of continuous in-gap state distribution responsible for the broadband luminescence in the CVD diamond films. Our ability to determine T_0 by fitting our data to Eq. (4) and the line-shape of the luminescence may indicate that the profile of the in-gap distribution is an exponential function. Srikanth *et al.* [37] have reported an in-gap exponential distribution of defect states of the form shown in Eq. (5). They deduced the existence of an exponential state distribution from conduction measurements in CVD diamond films. A comparitive study of PL and electrical conduction will be carried out by us to determine how the state distribution deduced from the PL measurements might affect the electrical transport in the CVD diamond films. Figure 12a and 12b represent schematically the density of the in-gap state distributions for the 20h and 40h samples respectively. The state distribution of the 20h sample is of lower density than that of the 40h sample but extends more widely into the band-gap of the diamond, implying a higher degree of randomness in this sample.

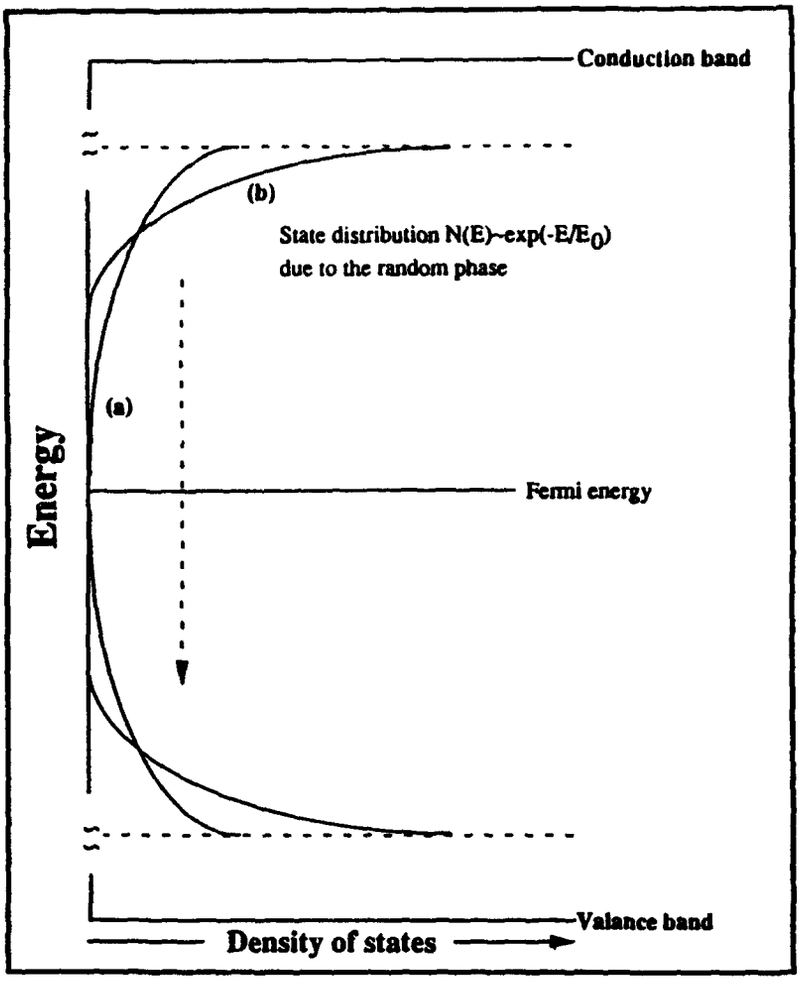

Figure 12. Schematic representation of the in-gap state distribution of (a) the 20h sample and (b) the 40h sample.

D. Conclusions

Raman and various photoluminescence techniques were employed in this paper to investigate the role of nitrogen-doping on the optical spectra of the CVD diamond films and to determine the origin of the broadband luminescence. Our experimental results suggest the following conclusions:

(a) The PL spectra of the 0.1% nitrogen-doped CVD diamond sample indicates that the incorporation of nitrogen into the diamond matrix introduces the optical centers at 2.154 eV and at 1.945 eV, and possibly introduces as well a new nitrogen-related center at 1.967 eV. The band A luminescence was also found in our PL spectra. The spectra of both nitrogen-doped and undoped films exhibit the broadband PL; the nitrogen-doped sample, however, has a line-shape distortion of the underlying broadband PL due to the vibronic interaction of the nitrogen centers.

(b) A higher percentage of nitrogen-doping results in a degradation of the diamond quality as indicated by the Raman spectra of the 2% nitrogen-doped sample. Furthermore, new features in the spectra were present and we speculate that they are due to nitrogen-carbon vibrational modes. Future work is in progress to investigate the influence of the percentage of nitrogen-doping on diamond quality.

(c) The temperature behavior of the broadband PL indicates that the band does not originate from a vibronic interaction. For the vibronic band, an increase in temperature would result in an increase in intensity and width. However, we found that the broadband PL in the CVD diamond films exhibits rather a decrease in intensity with increasing temperature without any change in width. Hence, we exclude the possibility of the broadband PL being due to any vibronic system of an electron-lattice coupling.

(d) The integrated intensity of the broadband PL was found to exhibit a temperature dependence charactertisic of optical emission from a continuous distribution of energy states. The temperature dependence of the PL was determined to follow the functional behavior described by Eq. (4) which is characteristic of an amorphous material [21]. In light of the above finding and from the correlation of the PL intensity to the sp^2 amorphous phase determined here and in our previous work [23], we suggest that the broadband PL in CVD diamond films is due to the optical transitions in an in-gap state distribution, where the in-gap state distribution is introduced by the amorphous phase of the sp^2 hybrid bondings.

(e) Our initial investigation into the characteristics of the in-gap state distribution suggest that it is of an exponential shape. It was found that the width as well as the density of the state distribution varied from sample to sample. These differences in the specifics of the state distribution are attributed to the film quality which in turn depends on the growth conditions.

E. Acknowledgment

This work was supported in part by the ONR through grant #N00014-93-1-0437. The authors wish to thank Terri McCormick and Andy Sowers for their contribution and technical support. Thanks are also extended to Brian Stoner for supplying some of the samples used in this research.

F. References

1. J. A. Freitas, Jr., J. E.Butler, S. G. Bishop, W. A. Carrington, and U. Storm, Mat. Res. Soc. Symp. Proc. **162**, 237 (1990).
2. Diane S. Knight and William B. White, SPIE **1055**, 144 (1989).
3. E. S Etz, E. N. Farabaugh, A. Feldman, and L. H. Robins, SPIE **969**, 86 (1988).
4. J. A. Freitas, Jr., J. E. Butler, and U. Storm, J. Mater. Res. **5**, 2502 (1990).
5. L. H. Robins, E. N. Farabaugh, and A. Feldman, SPIE **1325**, 130 (1990).

6. A. T. Collins and S. C. Lawson, J. Phys.: Condens. Matter **1**, 6929 (1989).
7. G. Davies and M. F. Hamer, Proc. R. Soc. Lond. A. **348**, 285 (1976).
8. A. T. Collins and K. Mohammed, J. Phys. C: Solid State Phys. **15**, 147 (1982).
9. Maria Estela Pereira, Maria Isabl B. Jorg, and Manuel F. Thomaz, J. Phys. C: Solid State Phys. **19**, 1009 (1986).
10. A. R. Badzian, T. Badzian, R. Roy, R. Messier, and K. E. Spear, Mater. Res. Bull. **23**, 531 (1988).
11. R. J. Nemanich, J. T. Glass, G. Lucovsky, and R. E. Shroder, J. Vac. Sci. Technol. A **6**, 1783 (1988).
12. Y. Sato and M. Kamo, Surf. Coatings Technol. **39/40**, 183 (1989).
13. J. Robertson, Advances In Physics **35**, 317 (1986).
14. J. Wagner and P. Lautenschlager, J. Appl. Phys. **59**, 2044 (1986).
15. R. Fang, Y. Song, M. Yang, W. Jiang, and K. Yan, J. Lumin. **40/41**, 905 (1988).
16. R. C. Fang, J. Lumin. **48/49**, 631 (1991).
17. S. H. Lin and B. J. Feldman, Phil. Mag. B **47**, 113 (1983).
18. N. F. Mott and E. A. Davis, *Electronic Processes in Non-Crystalline Materials* (Clarendon Press, Oxford, 1979).
19. J. M. Marshall and R. A. Street, Solid State Commun. **50**, 91 (1984).
20. B. Henderson and G. F. Imbusch, *Optical Spectroscopy of Inorganic Solids* (Clarendon Press, Oxford, 1989).
21. R. A. Street, in *Semiconductors and Semimetals*, edited by J. I. Pankove, vol.21, p. 197 (1984).
22. R. A. Street, Advances In Physics **30**, 593 (1981).
23. L.Bergman, B. R. Stoner, K. F. Turner, J. T. Glass, and R. J. Nemanich, J. Appl. Phys. **73**, 3951 (1993).
24. V. S. Vavilov, A. A. Gippius, A. M. Zaltsev, B. V. Deryagin, B. V. Spitsyn, and A. E. Aleksenko, Sov. Phys. Semicond. **14**, 1078 (1980).
25. J. Ruan, W. J. Choyke, and W. D. Partlow, Appl. Phys. Lett. **58**, 295 (1991).
26. J. Ruan, W. J. Choyke, and W. D. Partlow, J. Appl. Phys. **69**, 6632 (1991).
27. T. Feng and B. D. Schwartz, J. Appl. Phys. **73**, 1415 (1993).
28. John Walker, Rep. Prog. Phys. **42**, 1605 (1979).
29. A. T. Collins, J. Phys. C: Solid St. Phys. **13**, 2641 (1980).
30. Gordon Davies, in Chemistry and Physics of Carbon **13**, 2 (1977).
31. L. H. Robins, L. P. Cook, E. N. Farabaugh, and A. Feldman, Phys. Rev. B **39**, 13367 (1989).
32. K. V. Ravi, Materials Science and Engineering B **19**, 203 (1993).
33. R. J. Graham and K. V. Ravi, Appl. Phys. Lett. **60**, 1310 (1992).
34. Gordon Davies, Rep. Prog. Phys. **44**, 787 (1981).
35. D. Curie, *Luminescence in Crystals* (John Wiley and Sons, 1963).
36. G. S. Painter and D.E. Ellis, Phys.Rev.B **12**, 4747 (1970).
37. K. Srikanth, S. Ashok, A. Badzian, T. Badzian and R. Messier, Thin Solid Films **164**, 187 (1988).

VI. Growth and Characterization of Cubic Boron Nitride Thin Films*

D. J. Kester[a], K. S. Ailey, D. J. Lichtenwalner and R. F. Davis

Department of Materials Science and Engineering, North Carolina State University, Box 7907, Raleigh, North Carolina 27695

ABSTRACT

Boron nitride (BN) thin films have been grown on [100] oriented single crystals of Si, diamond, Cu and Ni substrates by ion beam assisted deposition (IBAD) using electron beam evaporation of boron together with simultaneous bombardment by nitrogen and argon ions. Characterization by FTIR and high resolution TEM showed that the films on Si and diamond consisted of initial non-cubic (amorphous and hexagonal BN) layers, followed by the growth of cubic(c)-BN. This growth sequence was attributed primarily to increasing compressive intrinsic stress with increased film thickness. Increasing the substrate temperature above 400°C led to the onset of c-BN at a greater film thickness, while increased ion flux resulted in earlier growth of this phase. These results may be explained by the relaxation of the intrinsic stress in the films at higher temperatures due to increased adatom mobility and to increased intrinsic stress in the films resulting from increased ion bombardment. Lower temperatures led to mixed phase growth. A minimum substrate temperature (200–300°C) is required for nucleation and growth of single phase c-BN by this techniques. It is believed that the interstitial Ar observed in RBS studies is primarily responsible for the stress generation in the films. A combination of h-BN and c-BN were deposited on Ni; only h-BN was obtained on Cu substrates.

A. Introduction

Boron nitride, like carbon, forms with three crystalline structures: a layered hexagonal form (h-BN) which is similar to graphite; cubic boron nitride (c-BN) which corresponds to diamond; and a rarer form, wurtzitic boron nitride (w-BN), which is analogous to Lonsdaleite. The last two phases are metastable at moderate temperatures and pressures.

The interest in c-BN films stems from their potential applications as hard coatings and from their electronic and thermal properties. Cubic BN is the hardest known material other than diamond. Unlike diamond, c-BN does not react with ferrous metals, and it can be used at

*Paper submitted to the Journal of Vacuum Science and Technology.

[a]Present address: Armstrong World Industries, Research and Development, P. O. Box 3511, Lancaster, Pennsylvania 17604

higher temperatures before the onset of structural transformation. These properties make it an excellent cutting tool material. Bulk c-BN crystals formed using high temperature-high pressure techniques are already used in the cutting tool industry. Electronic applications of cubic boron nitride would take advantage of its very wide band gap ($E_g \approx 6.4$ eV [1]), its ability to be doped both p-type and n-type with Be and Si, respectively [2], and for some applications its very high thermal conductivity.

Cubic boron nitride was first grown in bulk crystal form in 1956 [3]. Reports of c-BN in thin film form appeared as early as 1970 [4], but it was not until about 1987 that thin films conclusively characterized as cubic boron nitride were achieved [5]. Subsequently, many groups have successfully grown c-BN using various techniques including ion beam assisted deposition [6,7] r.f. sputtering [8], ion plating [9], laser ablation [10,11], ECR plasma [12], and chemical vapor deposition (CVD) [13].

Cracking and loss of adhesion of deposited c-BN films are frequently reported phenomena, which have been attributed to a high level of intrinsic compressive stress in the films [14,15]. Murakawa [9] has attempted to overcome this problem using buffer layers between the substrate and the BN film, including a graded B to BN layer and a TiN layer, together with post-deposition annealing of the films. Okamoto *et al.* [16] also used a graded B to BN buffer layer in CVD c-BN films. Both studies produced well adhered films. No reports have appeared of stress-free c-BN films grown directly on a substrate. By contrast, recent research strongly indicates that a high stress level in the film is a necessary condition for the formation of the cubic phase [15, 17].

An additional challenge is growing epitaxial films, which would be essential for the majority of electronic device applications. No reports of reproducible experiments of epitaxial growth of c-BN have appeared. A better understanding of what happens at the substrate-BN interface needs to be developed. In a previous paper [17] we have shown that when BN is deposited on Si, initial amorphous and hexagonal BN layers grow before cubic growth begins. If these interfacial layers are necessary precursors to c-BN growth, then it would appear exceedingly challenging to grow epitaxial c-BN using current PVD methods.

An area of research where significant progress has been made is in determining the deposition conditions necessary for c-BN growth. The work of Kester and Messier [18] established that for a given substrate temperature, the momentum transferred into the growing film by the bombarding ions is the single parameter which controls the formation of c-BN. As long as sufficient N is present, a threshold value of momentum transfer exists for the formation of c-BN. This controlling parameter incorporates the values of ion energy, ion flux, and ion species. As a result of the present study described below we have developed a better understanding of both the conditions required for c-BN growth and of the mechanisms responsible for that growth.

B. Experiment

Deposition. Ion beam assisted deposition (IBAD) has been used successfully for c-BN growth [17,18]. It is particularly useful in that the B deposition rate, bombarding ion energy, ion flux and ion species can be controlled and measured independently. This allows for good quantification of the deposition process. The IBAD configuration in the present study employed electron beam evaporation of boron together with simultaneous bombardment by nitrogen and argon ions from a Kaufman ion source. A schematic of the deposition system is shown in Fig. 1.

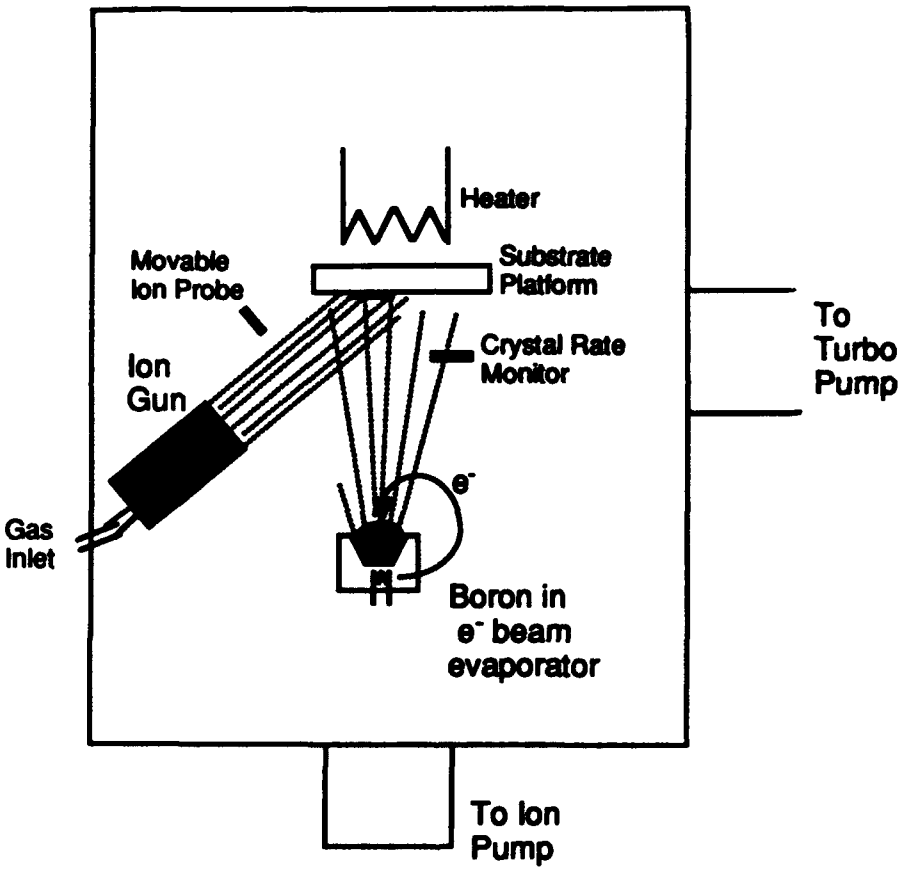

Figure 1. Schematic of UHV electron beam evaporator-based IBAD system used in this research.

The substrates used in this study were (100) single crystal infrared-transparent, high resistivity (ρ>50 Ω-cm) on-axis Si; cut and polished single crystal natural diamond; as well as polished single crystal Cu and Ni. The Si substrates were cleaned using a standard RCA procedure [19] of which the final step was a 5 min dip in 10% HF. This left the surface H terminated, as determined by XPS. The diamond substrates were etched in a boiling 3:4:1

H_2SO_4:HNO_3:$HClO_4$ solution for 45 minutes to remove any graphitic phase, and the Cu and Ni substrates were decreased ultrasonically in a sequence of TCE, acetone, methanol, and DI water. The substrates were attached to Mo holders using Ag paint which acted both as an adhesive and a thermal conductor. This assembly was subsequently loaded through a vacuum load lock into the UHV deposition chamber. Base pressures in the chamber were typically $5\text{-}8 \times 10^{-10}$ Torr.

Each substrate was heated using a W wire coil located behind the Mo substrate holder. They were baked under UHV conditions at 700°C for 20 min to remove residual H_2O and hydrocarbon species. The substrate temperature during deposition was monitored using thermocouples near the heater, the readings of which had been previously calibrated to several temperatures of the substrate surface. Boron was deposited using a constant deposition rate of 0.5 Å/s, which was monitored using a quartz crystal rate monitor. Fluxes of N and Ar ions were obtained from a 3 cm Ion Tech Kaufman source. Argon and nitrogen gases were used with a gas flow ratio of 1:1. Because of the close ionization potentials of these two gases, the ion ratio was also close to 1:1. The ion source was operated at 500 eV; based on the studies of Hubler *et al.* [20] the N ions were predominantly N_2^+. The discharge voltage of this source was maintained at a sufficiently low value to prevent double ionization of either species. Since it has been previously shown that c-BN can be successfully deposited using an Ar:N_2 ratio of 1:1 and an ion energy of 500 eV [17,18], these values were maintained constant throughout this study.

Both the ion beam and the boron evaporation were started and allowed to stabilize before deposition. During this period, the substrate was covered by a movable shutter. To eliminate the potential for surface damage, there was no pre-deposition ion bombardment of the substrates.

Characterization methods. The primary method of film characterization was Fourier transform infrared spectroscopy (FTIR) due to the ability to distinguish between the cubic and hexagonal or amorphous forms of BN. Cubic BN has a transverse optical mode absorption peak at 1075 cm^{-1}, while amorphous and hexagonal BN have a primary absorption peak at 1367 cm^{-1} and a secondary peak at 783 cm^{-1} [21,22]. The spectra were obtained using an Analect Instruments model fx-6260 spectrometer. The IR beam was passed through the BN coated substrate. A ratio of the resultant spectrum to that obtained from a background scan taken from an uncoated substrate was determined. Reflectance FTIR was employed to characterize the films deposited on the IR opaque Cu and Ni substrates. The latter study was conducted on a Nicolet 620 FTIR equipped with a Spectra Tech IR Plan optical microscope.

The film crystallography and the film-substrate interface were studied via high resolution cross sectional transmission electron microscopy (HRTEM) using a JEOL 4000EX operated at 400kV. The images were recorded using a 1mr convergence semi-angle at a Scherzer defocus of ~ 47nm. Samples were prepared using standard techniques [23].

Rutherford backscattering spectrometry (RBS) was used to measure the compositions and thicknesses of the films due to this techniques ability to give a depth profile of the film, not only information about the surface layer. 2.0 MeV primary He^+ ions and a 165° scattering angle were used for measuring the energy of the backscattered nuclei. The samples were tilted 6° to prevent channeling.

C. Results

FTIR Results. The results reported in this and the following subsection were obtained using only Si(100) substrates. To study the effect of substrate temperature (T_S) on the BN films, depositions were conducted from 200°C to 700°C. All other variables were held constant. The results of one of these series of depositions are shown in Fig. 2. There was almost no cubic phase in the 200°C film. In the temperature range of 300-400°C, the films

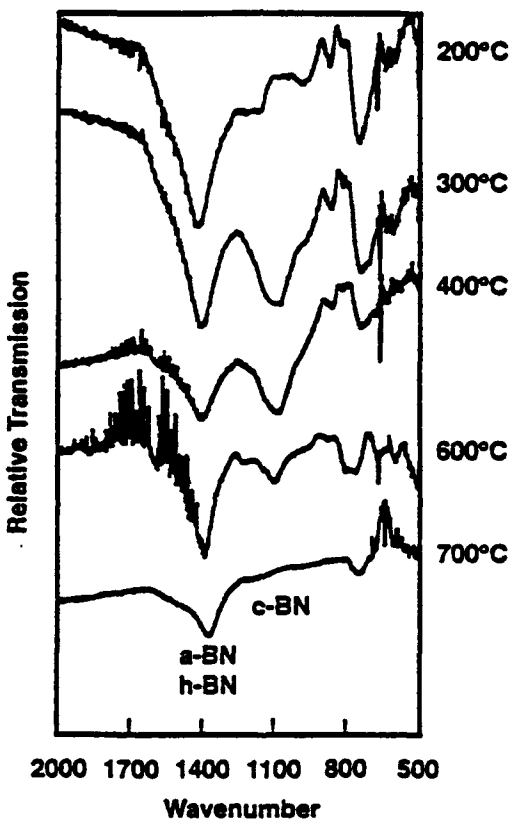

Figure 2. FTIR spectra of BN films deposited on Si(100) at various substrate temperatures. Other deposition conditions were film thickness: 200Å; ion flux: 0.32 mA/cm^2; boron deposition rate: 0.5 Å/s; ion energy: 500 eV; ion bombardment by 50:50 Ar:N_2.

were a mixture of the cubic and hexagonal/amorphous phases (IR does not distinguish between the hexagonal and amorphous forms of BN). The relative amount of cubic phase increased with increasing temperature. At some temperature above 400°C the amount of cubic phase began to drop rapidly; it was not observed at all in the film deposited at 700°C. These results correspond well with those of other researchers [24] who have also found that the best temperature for growing cubic boron nitride is at or close to 400°C.

A second significant parameter studied was the ion bombardment flux. As discussed above, it has been previously shown [18] that the critical parameter (at constant temperature) for growing the cubic phase is momentum, p, transferred from the bombarding ions into the growing film per deposited boron atom, p/a, where a is the boron flux measured in atoms $cm^{-2}\ s^{-1}$. This critical value is given by

$$\frac{p}{a} = \frac{J}{a}\sqrt{2m\gamma E} \tag{1}$$

where J/a is the ratio of bombarding ions to depositing boron atoms. J is the ion flux measured in ions $cm^{-2}\ s^{-1}$, m is the mass of the bombarding ions and E is their energy. The maximum energy transfer from the ion to the atom, γ, is given by

$$\gamma = \frac{4mM}{(m+M)^2} \tag{2}$$

with M being equal to the average mass of the atoms being bombarded. There is a linear relationship between the ion flux, J, and the momentum transfer value. Therefore a change in the ion flux (while keeping the ion energy and ion species distribution constant) acts directly as a change in momentum transfer. Since changing the ion energy, E, has less of an effect on the momentum (momentum being proportional to the square root of the energy), the bombardment level in this study was varied by varying the ion flux and keeping the ion energy constant.

Fig. 3(a) shows the effect of changing the ion flux while keeping the temperature constant at 600°C. Essentially no cubic phase is observed until the ion flux reaches 0.30 mA/cm^2. The small peaks observed at 1050–1100 cm-1 at the two lower flux values are due to the Si substrate. This confirms that there is a minimum momentum transfer level, and therefore ion flux, necessary to grow the cubic phase at a given temperature. The spectra shown in Fig. 3(b) are from films grown at the same conditions as those in Fig. 3(a), except at 400°C. There is a small cubic peak visible at 0.20 mA/cm^2, and the films are predominantly cubic at 0.24 and 0.30 mA/cm^2. Comparing Figs. 3(a) and (b) confirms the result seen in Fig. 2 that increasing the substrate temperature above 400°C lowers the proportion of cubic phase in the film.

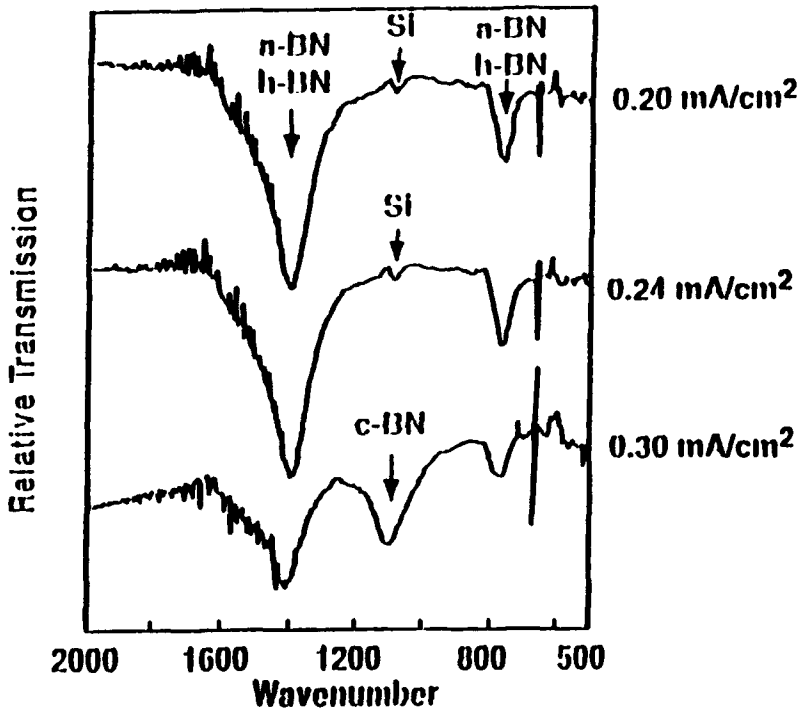

Figure 3 (a). FTIR spectra of a BN film deposited on Si(100) with various ion bombardment fluxes at a substrate temperatures of 600°C. Other deposition conditions were film thickness: 250Å; boron deposition rate: 0.5 Å/s; ion energy: 500 eV; ion bombardment by 50:50 Ar:N_2.

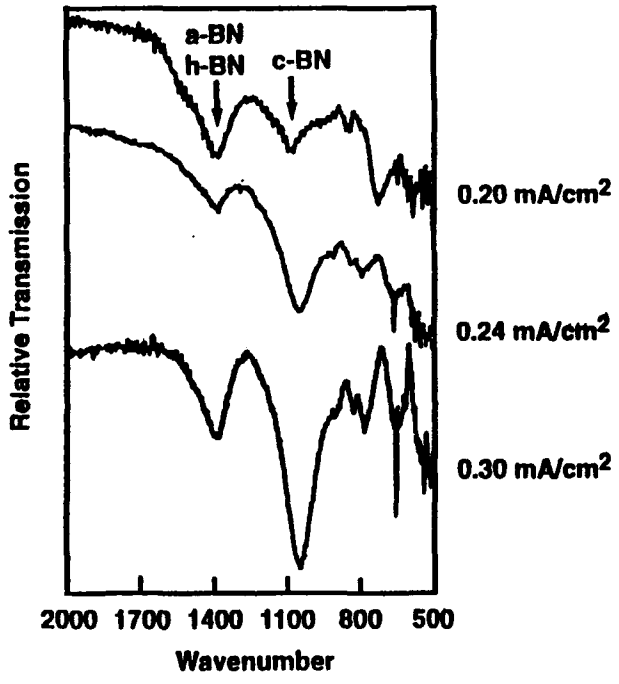

Figure 3 (b). FTIR spectra of a BN film deposited on Si(100) with various ion bombardment fluxes at a substrate temperatures of 400°C. Other deposition conditions were film thickness: 250Å; boron deposition rate: 0.5 Å/s; ion energy: 500 eV; ion bombardment by 50:50 Ar:N_2.

The data presented above indicated that increasing the ion flux, and thereby the momentum transfer, increases the amount of cubic phase in a film, and that increasing the substrate temperature above 400°C decreases the proportion of cubic phase. However, our previous FTIR and HRTEM results [17] showed that the relative amount of each phase in a 400°C film was also a function of film thickness. These films contained very thin amorphous and hexagonal layers of essentially constant thickness prior to the nucleation and growth of the c-BN layer. Nucleation of the pure cubic phase did not occur until a specific total thickness of the non-cubic phases was achieved.

As such, the FTIR spectra of films of different thicknesses deposited under identical conditions showed that the thicker films had a higher cubic to non-cubic ratio. Examination of films of different thicknesses prepared using the conditions of the 200Å thick 700°C film of Fig. 2, showed the same effect, as demonstrated in Fig. 4. The 100Å film and the 200Å films were completely amorphous/hexagonal, but the 400Å film was predominantly cubic. Similarly, FTIR of a set of films of different thicknesses prepared under the same conditions as the 600°C film of Fig. 2, revealed a growth sequence and layer thicknesses of non-cubic (<200Å), partially cubic (200Å), and predominantly cubic (remainder of film). These results indicate (and the HRTEM results noted below prove) that the different proportions of amorphous/hexagonal and cubic phase found in the different films are not due to different amounts of each phase interspersed through the film, but rather to the transition from single phase hexagonal to single phase cubic occurring at varying thicknesses depending on growth conditions. Specifically, the differences between the 400°C, 600°C, and 700°C films seen in Fig. 2, which ranged from significantly cubic at 400°C to completely non-cubic at 700°C are due to varying thicknesses at which the growth of the cubic phase layer begins. A higher substrate temperature delays the onset of the cubic phase. Increased ion flux enhances the onset of this phase.

HRTEM results. High resolution TEM images of films deposited at 200°C, 400°C, and 700°C are shown in Figures 5(a), 5(b), and 5(c). The film deposited at 200°C (Fig. 5(a)) has a 70Å amorphous layer at the Si interface followed by a layer of oriented h-BN. No c-BN is present. The film deposited at 400°C (Fig. 5(b)) has a 20Å amorphous layer followed by 50Å of oriented h-BN followed by c-BN. The film grown at 700°C (Fig. 5(c)) has a 50Å amorphous layer followed by a ~150Å layer of predominantly partially oriented h-BN material with a small amount of c-BN, followed by a c-BN layer.

RBS Results. The BN grown for RBS was deposited on the lower atomic number substrate of Be to circumvent overlap of the spectra of the Si substrate with that of the film. The deposition conditions were those which resulted in c-BN growth on Si: a substrate temperature of 400°C, ion energy of 500eV, and an ion flux of 0.24 mA/cm^2. The film thickness was 500Å. The results are shown in Fig. 6. Rutherford backscattering is more

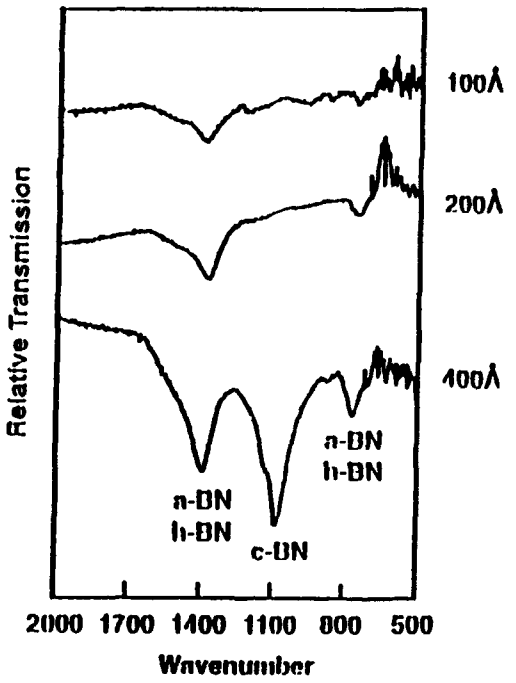

Figure 4. FTIR spectra of BN films deposited on Si(100) with various thicknesses. Other deposition conditions were substrate temperature: 700°C; ion flux: 0.32 mA/cm^2; boron deposition rate: 0.5 Å/s; ion energy: 500 eV; ion bombardment by 50:50 Ar:N_2.

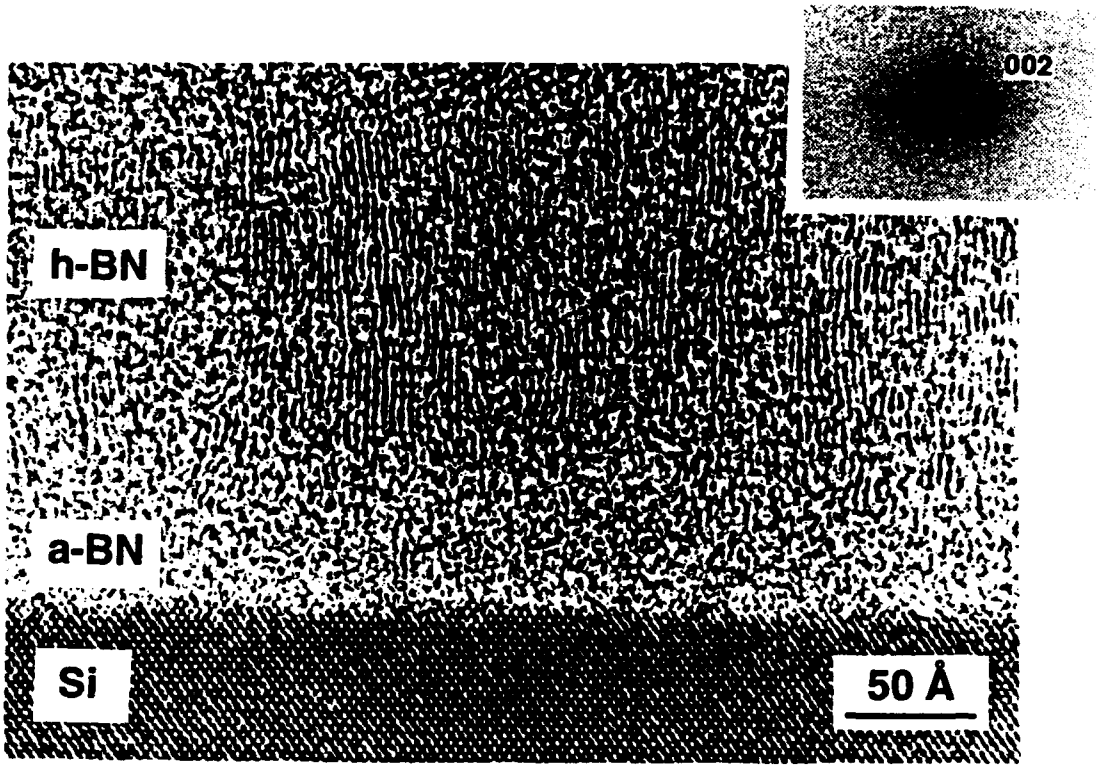

Figure 5(a). HRTEM image of a film deposited on Si(100) at 200°C. Other deposition conditions were ion flux: 0.28 mA/cm^2; boron deposition rate: 0.5 Å/s; ion energy: 500 eV; ion bombardment by 50: 50 Ar:N_2.

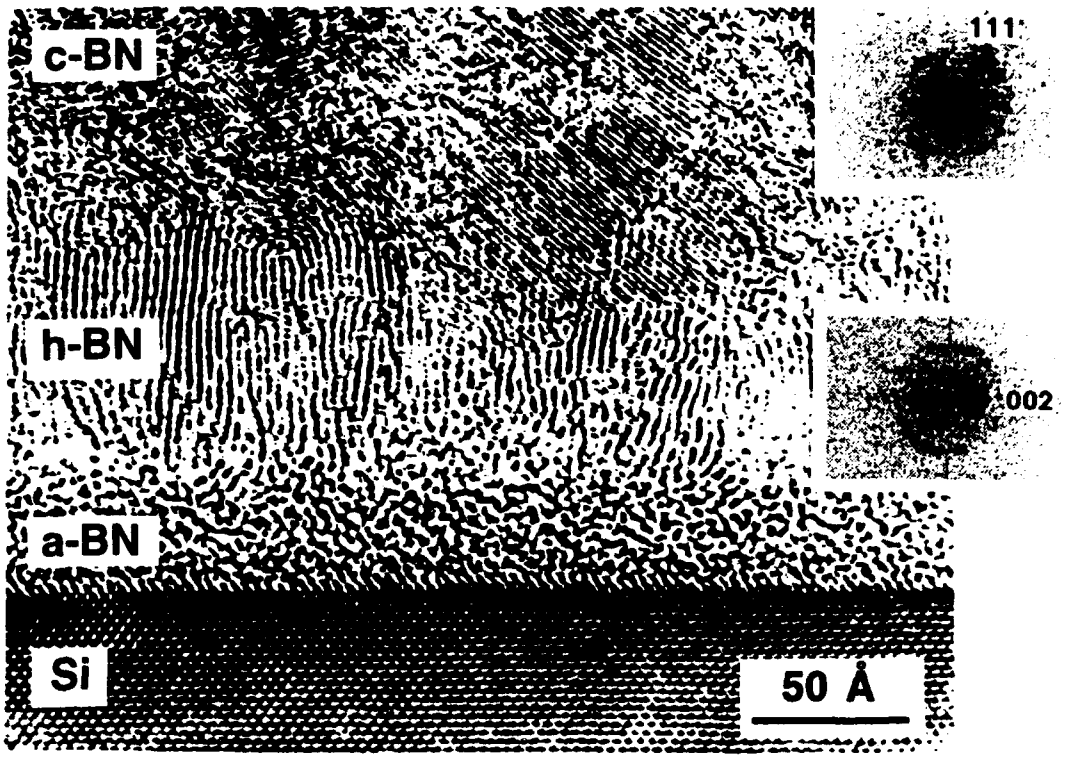

Figure 5(b). HRTEM image of a film deposited on Si(100) at 400°C. Other deposition conditions were ion flux: 0.12 mA/cm^2; boron deposition rate: 0.25 Å/s; ion energy: 500 eV; ion bombardment by 50: 50 Ar:N_2.

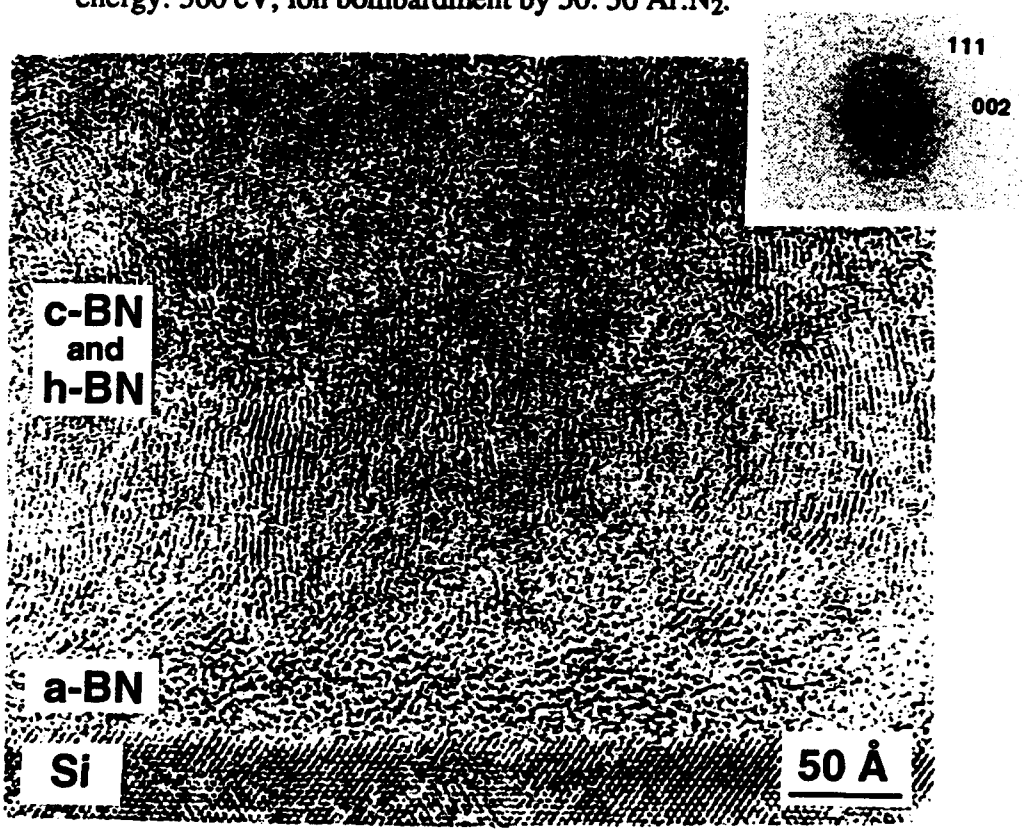

Figure 5(c). HRTEM image of a film deposited on Si(100) at 700°C. Other deposition conditions were ion flux: 0.28 mA/cm^2; boron deposition rate: 0.5 Å/s; ion energy: 500 eV; ion bombardment by 50: 50 Ar:N_2.

sensitive to elements of higher atomic number, due to their larger nuclear cross sections. Therefore, the sizes of the original peaks at various channel numbers do not directly show their actual concentration. Computer modeling of the spectra revealed that in addition to the expected Be, B, and N, there was O due to a BeO layer on the substrate as well as Ar, Fe, and Hf in the film having the atomic percentages of ~1.5%, ~0.2%, and ~0.05%, respectively. The Ar was derived from the ion bombardment during growth; the Fe was probably due to the ion beam bombardment of the stainless steel shutter above the substrates, and the Hf was very likely derived from resputtering of residual amounts previously deposited on the substrate block.

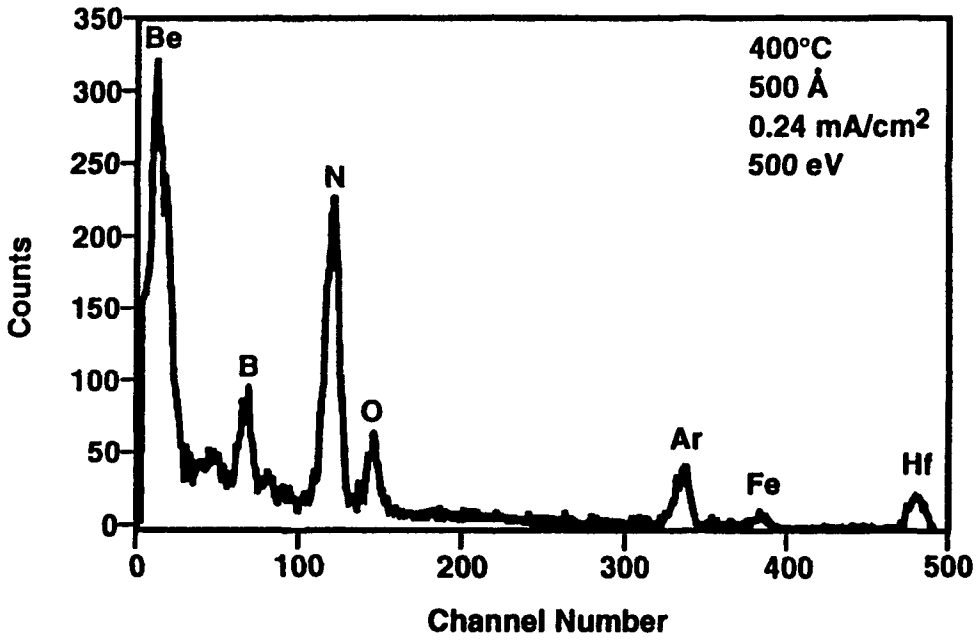

Figure 6. RBS spectra of a BN film on a beryllium substrate. Deposition conditions were film thickness: 500Å, substrate temperature: 400°C; ion flux: 0.24 mA/cm^2; boron deposition rate: 0.5 Å/s; ion energy: 500 eV; ion bombardment by 50:50 Ar:N_2.

Other Substrates. Films having a thickness of 1000 Å were grown on diamond at substrate temperatures of 400° and 600°C using an ion energy of 500eV and an ion flux of 0.24 mA/cm^2. A representative FTIR pattern of one of the films deposited at 400°C is shown in Fig. 7. A sharp c-BN peak is observed at ~1080 cm^{-1}. The h-BN peak is very small. The spectrum of this relatively thick film has a sharper c-BN peak and a better c-BN to h-BN ratio than any of the films we had previously deposited on Si, and is as good or better than any that have previously appeared in the literature. For the film grown at 600°C the FTIR spectrum was essentially the same.

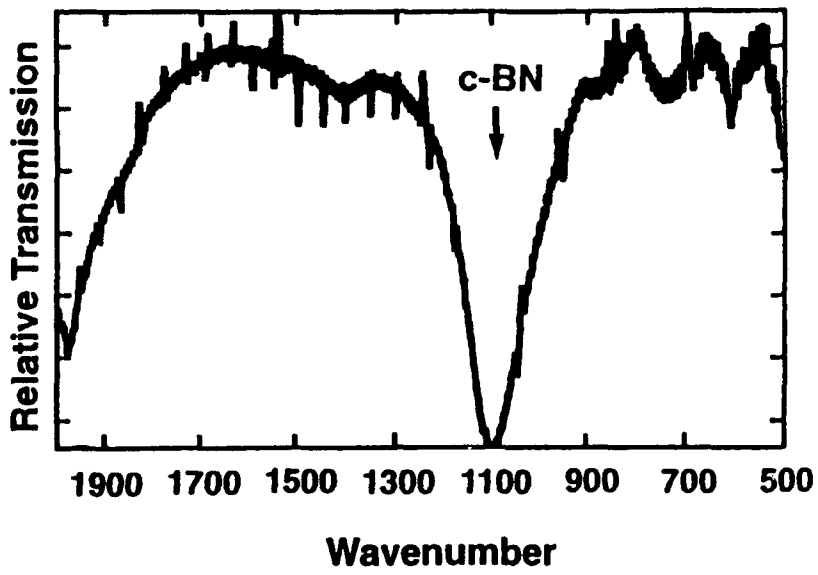

Figure 7. FTIR spectra of BN deposited on a single crystal diamond(100) substrate. Deposition conditions were film thickness: 1000Å, substrate temperature: 400°C; ion flux: 0.24 mA/cm^2; boron deposition rate: 0.5 Å/s; ion energy: 500 eV; ion bombardment by 50:50 Ar:N_2.

Observation via SEM of the films deposited at 400°C showed occasional cracking. The films deposited at 600°C showed no cracking or delamination. Films deposited under the same deposition conditions and the same thicknesses on Si exhibited both severe cracking and delamination.

High resolution TEM was performed on the sample grown at 600°C, and an image is shown in Fig. 8. The same type of layered structure observed on BN grown on Si is present, although not as pronounced.

Nickel and Cu also have lattice spacings very close to that of c-BN, with a lattice mismatch for Ni of 2.6% and for Cu of less than 0.05%. Therefore it was thought that like diamond (which has a lattice mismatch of 1.4%) they may be better substrates for c-BN growth than Si which has a lattice mismatch of 33%. Films having a thickness of 500Å were grown at 400°C under the same conditions of ion flux and ion energy employed in the deposition on diamond. As shown in Fig. 9, reflectance FTIR from films grown on the Ni substrate revealed a mixture of h-BN and c-BN; films grown on Cu were h-BN with no evidence of c-BN.

D. Discussion

The above results show that the onset of c-BN growth is a function of temperature, ion momentum transfer and deposition period (film thickness). McKenzie *et al.* [14,15] have shown theoretically and experimentally that the effect of deposition period is caused by the build-up of biaxial compressive stresses in the growing film. They observed by FTIR,

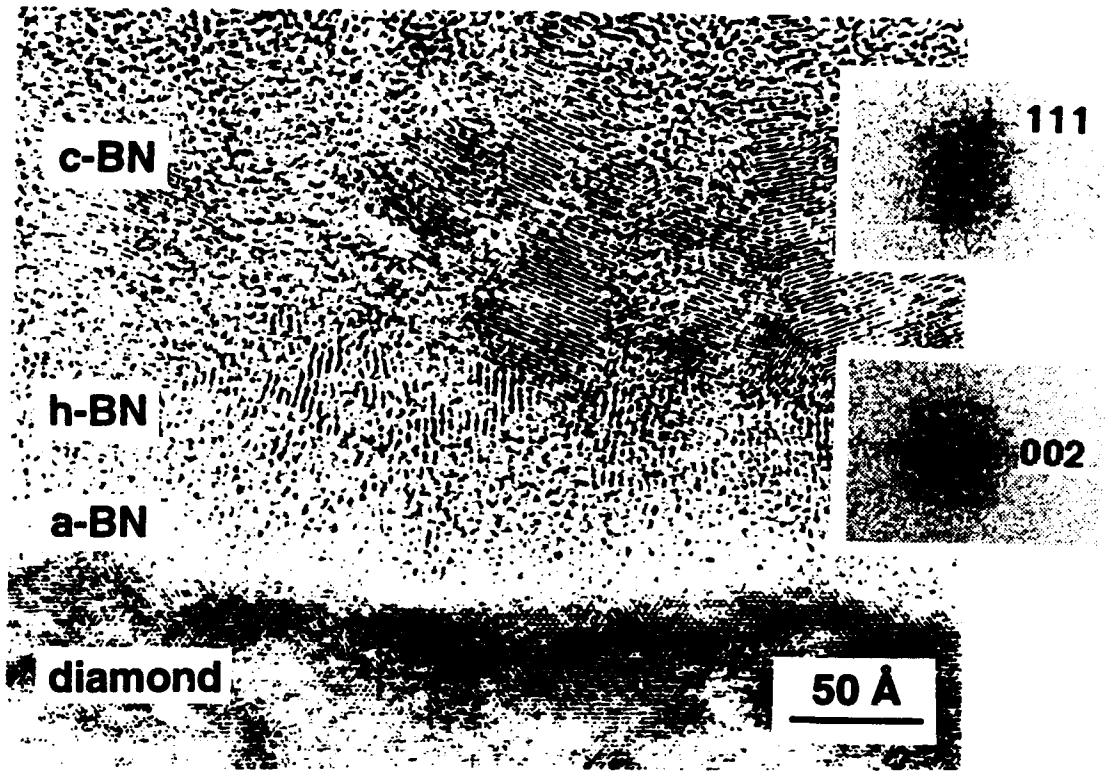

Figure 8. HRTEM image of a 600°C film on a diamond(100) substrate. Other deposition conditions were ion flux: 0.28 mA/cm^2; boron deposition rate: 0.5 Å/s; ion energy: 500 eV; ion bombardment by 50:50 Ar:N_2.

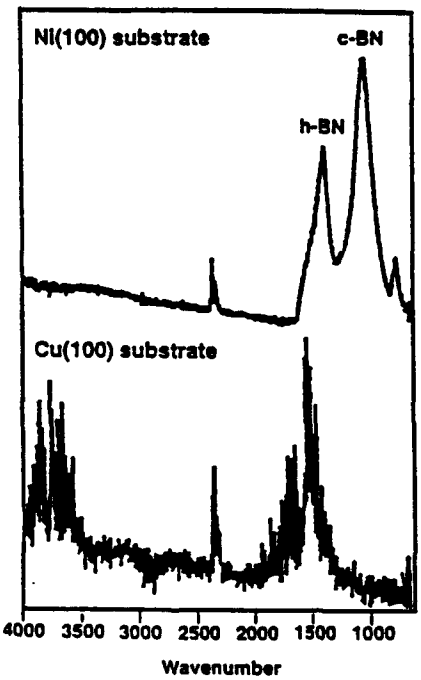

Figure 9. Reflectance FTIR of BN deposited on Cu(100) and Ni(100) substrates. Deposition conditions were film thickness: 500Å, substrate temperature: 400°C; ion flux: 0.24 mA/cm^2; boron deposition rate: 0.5 Å/s; ion energy: 500 eV; ion bombardment by 50:50 Ar:N_2.

electron energy loss spectroscopy and TEM an initial layer of h-BN oriented perpendicular to the substrate surface. The nucleation and growth of c-BN occurred as the stress in the film increased. No amorphous phase was reported. The stress at the onset of c-BN growth corresponded to conditions in the high pressure regime where this phase is stable. The present results can be understood using this model. Increasing the substrate temperature from, for example, 400°C to 700°C, results in both a higher surface mobility of the adsorbed species and possibly bulk annealing, which allow stress relaxation. Thus, as shown in Fig. 4, the higher the deposition temperature the greater the film thickness necessary to reach the stress level required for c-BN nucleation and growth, all other conditions being the same. There is a sharp increase in the transition thickness, and therefore a sharp drop in stress, within the 600-700°C temperature range. This corresponds with the results of Windischmann [25] who found in several different materials, that increasing the deposition temperature from room temperature causes a gradual decrease in the intrinsic stress , followed by a sharp drop when the temperature reaches $T_m/3$, where T_m is the melting point. For BN, $T_m/3$ is ~700°C.

The foregoing explanation does not account for the results of decreasing the temperature below 400°C, for it does not further lower the threshold thickness for initiation of the cubic phase. In fact, at these lower temperatures, growth of the cubic material as a single phase was not observed. The existence of an apparent minimum in substrate temperature for the growth of pure c-BN indicates that the combination of thermal energy and intrinsic stress is insufficient for all the B and N atoms to surmount the activation energy barrier between the layered h-BN and the three-dimensional c-BN structure.

Similarly, an increase in ion flux and momentum transfer into the growing film will lead to a more rapid increase in stress, as shown by Kester and Messier [18] as well as Windischmann [25] and a decrease in the film thickness necessary for the initiation of the cubic phase. The results presented in Figs. 3(a) and (b) show the onset of c-BN to be also a function of ion flux. These correspondences between known effects on stress and the onset of c-BN growth are strong evidence that the cubic phase growth results directly from stress.

The mechanism(s) which cause(s) the increase in stress in the films is not completely understood. It may be densification due to ion bombardment, as reported by [27]. The densification occurs through the collapse of the void structure found in non-bombarded films. Nir [28] and Targove and Macleod [29] have shown experimentally that the magnitude of the compressive stress is a function of the momentum transfer to the growing surface for particle energies <1kV. Theoretical studies by Windischmann [30] support these findings. A second possibility is that the stress is due to the presence of interstitials in the film. In the case of the c-BN films, the relatively high concentration of Ar (1.5 at.%) as shown by RBS would suggest that the compressive stress may be caused by interstitial Ar atoms in the manner observed by McKenzie *et al.* [14].

In the growth of BN films via IBAD by Stambouli et. al. [31] using bombardment with nitrogen ions, it was found that sufficient bombardment by nitrogen ions resulted in nitrogen-rich (non-cubic) BN_{1+x} films with a higher density than stoichiometric BN films. The former also possessed significantly higher compressive stresses than the stoichiometric films. They attributed this to interstitial N. If this is the case, bombardment by the larger Ar ion, and the formation of interstitial Ar at 1.5 at.%, would be expected to also increase the compressive stress in the films. In fact, Fahnline *et al.* [32] showed that 1.5 at.% Ar in Ge films caused a significant increase in compressive intrinsic stress.

Kester and Messier [18] previously showed that the phase of BN films is determined by three factors: substrate temperature, bombardment measured in terms of momentum transfer, and stoichiometry. The stoichiometry factor was a requirement in that at least one bombarding N atom had to be present for each depositing B atom. They plotted the observed phase(s) as a function of temperature and bombardment. In the present study we have shown that these are controlling parameters, but they control not only whether or not cubic growth will occur, but the time of nucleation and growth of this phase. Some of the conditions that they described as leading to mixed cubic and hexagonal growth appear to be conditions leading to layered single phase hexagonal followed by single phase cubic growth.

The problem of adhesion of c-BN on Si was addressed by using substrates with better lattice matching to c-BN including Cu and Ni and diamond. The cubic phase did not grow on the Cu(100) substrate due to its excellent ductility which adsorbed the stresses generated in the growing film ; it did grow on the less ductile Ni(100) substrate, but the adhesion was as poor as on Si. These results indicate that the adhesion problem is not simply one of lattice mismatch with the substrate.

Adhesion on the diamond substrates was much better than on the other materials. Although a relatively small number of samples were produced, due to the prohibitive cost, these results suggest that c-BN does not easily grow initially on diamond even though this substrate has a higher surface energy than c-BN. Moreover, these results imply that c-BN will not initially deposit on any material, at least by the methods used in this investigation.

E. Conclusions

Boron nitride films deposited using ion beam assisted deposition on Si, diamond and Ni substrates grow in a sequence of amorphous, hexagonal and cubic layers. This is believed to be caused primarily by the increased incorporation of intrinsic biaxial compressive stresses in the films. The nucleation of the cubic phase occurs at differing film thicknesses as a function of both substrate temperature and ion flux. There appears to be a minimum substrate temperature (200–300°C) below which single phase growth of c-BN does not occur. At higher temperatures the onset of the cubic phase is a function of temperature, appearing at

greater thicknesses at higher temperatures under the same ion flux. This is attributed to increased adatom mobility and bulk annealing with increasing temperature and a concomitant relaxation of stress. For these reasons the optimum temperature range for the growth of c-BN was determined to be 400-500°C. This range in T is similar to that determined by other investigators. Increased ion bombardment, as measured by momentum transferred into the film, leads to an earlier start of cubic growth, apparently due to the increased stress. It is suggested that the stress in the films may be due to Ar interstitials. The fact that stress is a function of momentum transferred into the film may be due to higher momentum bombardment (higher flux, energy or ion mass) leading to deeper and/or a greater number of interstitials.

We were unable to nucleate c-BN as the initial phase on any substrate; we suspect that this may prove difficult using bombardment based deposition methods due to the requirement of increasing stress generation in the films.

E. Acknowledgements

The authors express their appreciation to the Electronic Materials Center of Kobe Steel, USA and the Strategic Defense Initiative via the Office of Naval Research (Contract No. N00014-92-J-1720) for support of this research, to Dr. Nalin Parikh of the University of North Carolina-Chapel Hill for the RBS measurements, to Professor D. R. McKenzie of the University of Sydney and Lisa M. Porter, R. C. Glass and M. J. Paisley of NCSU for helpful discussion.

F. References

1. L. Vel, G. Demazeau, and J. Etourneau, Materials Science and Engineering B10, 149 (1991).
2. K. Era, O. Mishima, Y. Wada, J. Tanaka, and S. Yamaoka, in Electroluminescence, edited by S. Shionoya and H. Kobayashi, Springer Proceedings in Physics, Vol. 38, 386 (1989).
3. R. H. Wentorf, Jr., J. Chem. Phys. 26, 956 (1957).
4. V. N. Gashtold *et al.*, Elektronnaya Tekhnika 12, 58 (1970).
5. K. Inagawa, K. Watanabe, H. Ohsone, K. Saitoh, and A. Itoh, J. Vac. Sci. Technol. A5, 2696 (1987).
6. D. J. Kester and R. Messier, Mater. Res. Soc. Symp. Proc. 235, 721 (1992).
7. T. Wada and N. Yamashita, J. Vac. Soc. Technol. A10, 515 (1992).
8. K. Bewilogua, J. Buth, H. Hübsch, and M. Grischke, Diamond and Related Materials 2, 1206 (1993).
9. M. Murakawa, S. Watanabe, and S. Miyake, Diamond Films and Technol. 1, 55 (1991).
10. G. L. Doll, J. A. Sell, C. A. Taylor II, and R. Clarke, Phys. Rev. B 43, 6816 (1991).
11. T. A. Friedmann, K. F. McCarty, and E. J. Klaus, Applied Physics Letters 61, 2406 (1992).
12. Y. Osaka, M. Okamoto, and Y. Utsumi, Mater. Res. Soc. Symp. Proc. 223, 81 (1991).
13. H. Saitoh and W. Yarborough, Applied Physics Letters 58, 2228 (1991).
14. D. R. McKenzie, W. D. McFall, W. G. Sainty, C. A. Davis and R. E. Collins, Diamond Relat. Mater. 2, 970 (1993).

15. D. R. McKenzie, J. Vac. Sci. Technol. A11,2758 (1993).
16. M. Okamoto, H. Yokoyama, and Y. Osaka, Japanese Journal of Applied Physics 29, 930 (1990).
17. D. J. Kester, K. S. Ailey, R. F. Davis, and K. L. More, J. Mater. Res. 8, 1213 (1993).
18. D. J. Kester and R. Messier, J. Appl. Phys. 72, 504 (1992).
19. W. Kern and D. A. Puo-tinen, RCA Rev. 31, 187 (1970).
20. D. Van Vechten, G. K. Hubler, and E. P. Donovan, Vacuum 36, 841 (1986).
21. R. Geick and C. H. Perry, Phys. Rev. 146, 543 (1966).
22. P. J. Gielisse, S. S. Mitra, J. N. Plendl, R. D. Griffis, L. C. Mansur, R. Marshall, and E. A. Pascoe, Phys. Rev. 155, 1039 (1967).
23. C. H. Carter, Jr., J. A. Edmond, J. W. Palmour, J. Ryu, H. J. Kim and R. F. Davis in *Microscopic Identification of Electronic Defects in Semiconductors*, edited by N. M. Johnson, S. G. Bishop, and G. Watkins (Mater. Res. Soc. Proc., 46, Pittsburgh, PA 1985) pp. 593 -598.
24. N. Tanabe, T. Hayashi, and M. Iwaki, Diamond and Related Materials 1,151 (1992).
25. H. Windischmann, J. Vac. Sci. Technol. A7, 2247 (1989).
26. H. Windischmann, J. Appl. Phys. 62, 1800 (1987).
27. R. A. Roy and D. S. Yee, in *Handbook of Ion Beam Processing Technology*, edited by J. J. Cuomo, S. M. Rossnagel, and H. R. Kaufman, (Noyes, Park Ridge, NJ, 1989).
28. D. Nir, J. Vac. Sci. Technol. A4, 2954 (1986).
29. J. D. Targove and H. A. Macleod, App. Optics 27, 3779 (1991).
30. H. Windischmann, J. Vac. Sci. Technol. A9, 2431 (1991).
31. V. Stambouli, O. Burat, D. Bouchier, and G. Gautherin, Surface and Coatings Technology 43/44, 137 (1990).
32. D. Fahnline, B. Yang, K. Vedam, R. Messier, and L. Pilione, Mater. Res. Soc. Symp. Proc. 130, 355 (1989).

VII. Distribution List

Mr. Max Yoder
Office of Naval Research
Electronics Program–Code 314
Ballston Tower One
800 North Quincy Street
Arlington, VA 22217-5660

Office of Naval Research
Resident Representative
The Ohio State Univ. Research Center
1960 Kenny Road
Columbus, OH 43210-1063

Director
Naval Research Laboratory
Attention: Code 2627
Washington, DC 20314

Defense Technical Information Center
Building 5
Cameron Station
Alexandria, VA 22314

Robert J. Markunas
Research Triangle Institute
Post Office Box 12194
Research Triangle Park, NC 27709-2194

Dr. Ron Rudder
Research Triangle Institute
P. O. Box 12194
Research Triangle Park, NC 27709-2194

Howard Schmidt and Mark Hammond
Schmidt Instruments
2476 Bolsover, Suite 234
Houston, TX 77004

Prof. Karl Spear
Pennsylvania State University
201 Steidle
University Park, PA 16802

Michael W. Geis
Lincoln Laboratories
244 Wood Street
P. O. Box 73
Lexington, MA 02173

Professor R. F. Davis
Materials Science and Engineering
Box 7907
North Carolina State University
Raleigh, NC 27695-7907

Professor R. J. Nemanich
Department of Physics
Box 8202
North Carolina State University
Raleigh, NC 27695-8202

Professor John C. Angus
Chemical Engineering
Case Western Reserve University
Cleveland, OH 44106

Dr. Andrzej Badzian
271 Materials Research Laboratory
The Pennslyvania State University
University Park, PA 16802

Dr. H. Liu
Emcore Corp.
35 Elizabeth Avenue
Somerset, NJ 08873

Prof. Karen Gleason
Chemical Engineering, Rm. 66-462
M. I. T.
Cambridge, MA 02134

Prof. Jerry Whitten
Chemistry
Box 8201
N. C. State University
Raleigh, NC 27695-8201

Dr. Ray Thomas
Research Triangle Institute
Box 12194
Research Triangle Park, NC 27709-2194

Allen R. Kirkpatrick
Epion Corp.
4R Alfred Circle
Bedford, MA 01730

Robert C. Linares
Linares Management Assoc., Inc.
P. O. Box 336
Sherborn, MA 01770

Dr. Martin Kordesch
Physics
Clippinger Research Laboratories
Ohio University
Athens, OH 45701-2979

Prof. Charter Stinespring
Chemical Engineering, Box 6101
West Virginia University
Morgantown, WV 26506

Robert Hauge
Chemistry
Rice University
Houston, TX 77251

Dr. John Margrave
HARC
4800 Research Forest Drive
The Woodlands, TX 77381

Dr. John Posthill
Research Triangle Institute
P. O. Box 12194
Research Triangle Park, NC 27709-2194

Dr. James Butler
NRL Code 6174
Washington, DC 20375

Dr. Andrew Freedman
Aerodyne Research, Inc.
45 Manning Road
Billerica, MA 01821

Prof. Michael Frenklach
Penn State University
202 Academic Projects Bldg.
University Park, PA 16802

Prof. Jeffrey T. Glass
Materials Science & Engr.
Box 7907
North Carolina State University
Raleigh, NC 27695-7907

Dr. Warren Pickett
NRL Code 4692
Washington, DC 20375-5000

Prof. Max Swanson
Physics
University of North Carolina
Chapel Hill, NC 27599-3255

Dr. James Zeidler
Code 7601
NRaD
San Diego, CA 92152